

12-2015

TRACKING ANISOTROPIC OPTICAL TRACERS TO STUDY BIOPHYSICAL PROCESSES AND CYTOTOXICITY

Khanh Van Nguyen

Clemson University, khanhvn@g.clemson.edu

Follow this and additional works at: https://tigerprints.clemson.edu/all_dissertations

 Part of the [Chemistry Commons](#)

Recommended Citation

Nguyen, Khanh Van, "TRACKING ANISOTROPIC OPTICAL TRACERS TO STUDY BIOPHYSICAL PROCESSES AND CYTOTOXICITY" (2015). *All Dissertations*. 1545.

https://tigerprints.clemson.edu/all_dissertations/1545

This Dissertation is brought to you for free and open access by the Dissertations at TigerPrints. It has been accepted for inclusion in All Dissertations by an authorized administrator of TigerPrints. For more information, please contact kokeefe@clemson.edu.

TRACKING ANISOTROPIC OPTICAL TRACERS TO STUDY BIOPHYSICAL
PROCESSES AND CYTOTOXICITY

A Dissertation
Presented to
the Graduate School of
Clemson University

In Partial Fulfillment
of the Requirements for the Degree
Doctor of Philosophy
Chemistry

by
Khanh Van Thi Nguyen
December 2015

Accepted by:
Dr. Jeffrey N. Anker, Committee Chair
Dr. Julia Brumaghim
Dr. Kenneth A. Christensen
Dr. Jason D. McNeill

ABSTRACT

We use anisotropic optical tracers (also called magnetically modulated optical nanoprobes – MagMOONs or MOONs for non-magnetic nanoprobes in this dissertation) to study biophysical processes such as enzyme-catalyzed cleavage through tissue, intracellular transport of these tracers and cytotoxicity based on this transport. The anisotropic optical properties cause these tracers to blink when rotating. This blinking is distinguishable from the background and can be tracked on a single-particle level in the absence of tissue, or for an ensemble average of tracers blinking through tissue. An alginate gel containing these tracers in the form of a thin film can be used as a sensor to detect alginate lyase, a protease of alginate gel. As the protease cleaves the gel, the tracers are released, free to rotate and give a blinking signal that can be tracked under the microscope. The tracers started blinking approximately 10 minutes after 2 mg/mL alginate lyase addition, and this blinking was clearly detected through up to 4 mm of chicken breast. Similar tracer-integrated gel films may potentially be employed to detect bacterial biofilm formation on medical implants by sensing specific proteases that either activate a related function or regulate biofilm formation. It can also be applied to other biosensors and drug delivery systems based on enzyme-catalyzed breakdown of gel components.

For intracellular transport and cytotoxicity, we apply the advantages of rotational and translational single particle tracking in cytotoxicity studies by observing the tracers' behavior with and without the presence of toxic substances. Both cyanide and 2-deoxy-D-glucose or azide and 2-deoxy-D-glucose combinations immediately inhibited

intracellular motion in J774A.1 macrophages upon addition. This result suggested our method can potentially be applied to study cytotoxicity of particulate matter. More importantly, tracking simultaneously the tracers' translation and rotation reveals interesting information about macrophage intracellular transport; for instance, tracers do not rotate when sliding along microtubules. The data analysis also confirmed that sliding periods contributed to a major portion of total movement but comprised a very small portion of total observation time.

DEDICATION

This work is dedicated to my parents, Mr. Nguyễn Văn Thịnh and Mrs. Lê Thị Đon, who have always supported me and been my source of energy, and my brother Nguyễn Tuấn Anh who first introduced me to the world of Science and Chemistry.

ACKNOWLEDGMENTS

I would like to specially thank my advisor-mentor, Dr. Jeffrey Anker, for his continuing guidance and support throughout my time doing research work at Clemson University. I also thank Dr. Julia Brumaghim, Dr. Kenneth Christensen and Dr. Jason McNeill for being in my committee. I have learned from them the scientific way of thinking, reasoning, and problem solving. I thank the Chemistry Department and the Vietnam Education Foundation for the fellowship that brought me to the U.S from Vietnam. Last but not least, I thank my friends in the Anker's group, especially Dr. Fenglin Wang, Melissa Rolgaski, Donald Benza, Dr. Fathima Ameer, Gretchen Schober, Unaiza Uzair, Dr. Hongyu Chen, and all the people I met at Clemson, specially Nhu-Y Phan-Thien, Yamin Htet, Mioko Tamura, Liem Nguyen, Thanh To, and Maria Mullet, who have shared with me the graduate school life.

This research work was supported by the NIH NIBIB grant award number 1R15EB014560-01A1; the South Carolina Research Authority NSF grant 2002-593TO#0056 for the magnetic field control; the Spherotech Inc. for the magnetic fluorescent particles, and the Vietnam Education Foundation for a fellowship to Khanh Van Thi Nguyen.

TABLE OF CONTENTS

	Page
TITLE PAGE	i
ABSTRACT	ii
DEDICATION	iv
ACKNOWLEDGMENTS	v
LIST OF TABLES	viii
LIST OF FIGURES	ix
CHAPTER	
I. INTRODUCTION	1
Lung Particle Toxicity	2
Live/Dead Assays and Cytomagnetometry Approach to Study Cytotoxicity	4
Single Particle Tracking, SPORT, and our Approach to Study Cytotoxicity with Anisotropic Optical Tracer Tracking	9
II. TRACKING MAGMOONS TO DETECT GELATION AND DE-GELATION	16
Introduction	16
Method and Experimental Setup	22
Results and Discussion	29
Conclusions and Future Work	44
III. TRACKING ANISOTROPIC OPTICAL TRACERS (MOONS) TO STUDY INTRACELLULAR TRANSPORT AND CYTOTOXICITY	45
Introduction	45
Method and Experimental Setup	52
Results and Discussion	55
Conclusions and Future Work	68

Table of Contents (Continued)

	Page
IV. SUMMARY AND FUTURE WORK	69
APPENDICES	71
A: Poster: Using magnetic particle tracking to study rotational transport in macrophages	72
B: Poster: Magnetically modulated single particle tracking as a tool to study cytotoxicity of airborne nanoparticles.....	73
C: Matlab Script for Particle Tracking	74
D: Matlab Script for MSD Calculation.....	76
E: Matlab Script for Motion Classification	78
F: License Agreement	80
REFERENCES	81

LIST OF TABLES

Table		Page
3.1	Motion characterization: D , v and α	66
3.2	Motion characterization: Percentage of confined, diffusive and directed motion.....	68

LIST OF FIGURES

Figure		Page
2.1	Experimental setup.....	27
2.2	Summary of gelation and de-gelation experiments	29
2.3	Tracking individual MagMOONs to detect alginate de-gelation by ammonium replacement.....	32
2.4	Tracking individual MagMOONs to detect alginate de-gelation by alginate lyase.....	34
2.5	Fluorescent imaging through turbid chicken breast tissue.....	37
2.6	Monitoring of MagMOON modulation through tissue after adding denatured and active lyase to the alginate gel	39
2.7	Detection through tissue the de-gelation by alginate	42
2.8	Fourier transform analysis to detect blinking through different tissue thickness	43
3.1	Superimposed image of macrophages in transmitted light bright field (gray) and fluorescence from MOONs (red).....	56
3.2	Position and intensity change of a single MOON particle with time	58
3.3	Correlation between velocity and intensity change of MOONs in cells (a), in glycerol (b), and by simulation (c).....	60
3.4	Trajectories of MOONs in macrophages with (NaN ₃ + 2-deoxy-D-glucose) addition (a) and no toxin addition (b)	62
3.5	MSD curves of simulated Brownian motion (a), motion in cell with no toxin addition (b) and motion in cells with toxin addition (c)..	65
3.6	Motion characterizations based on α	67

CHAPTER ONE

INTRODUCTION

This dissertation describes some applications of anisotropic optical tracers to study different biophysical processes such as the enzyme-catalytic cleavage under tissue (Chapter Two), the intracellular transport and the cytotoxicity based on that transport observation (Chapter Three).

In the introduction chapter (Chapter One), the potential toxicity of lung particulate matters and its study need, and some proposed mechanisms for the toxicity of these particles will firstly be presented. Different approaches to study cytotoxicity including conventional live/dead assays and the *in vivo* cytomagnetometry methods developed by Möller, Nemoto and others will then be summarized. Lastly, our novel approach of using anisotropic optical tracers together with the single particle tracking technique to study cytotoxicity will be introduced.

Chapter Two demonstrates in principle the through-tissue detection of enzyme or protease activity by tracking single anisotropic optical tracers, to study chemically induced viscosity change processes. This technique can be employed to detect bacterial biofilm formation on medical implants or other biosensors and drug delivery systems based on enzyme-catalyzed breakdown of gel components.

Chapter Three describes the application of anisotropic optical tracer tracking in intracellular transport study as an approach to investigate cytotoxicity, and Chapter Four summarizes these results and suggests future work.

Lung Particle Toxicity

The rapid development of nanomaterials in industry and medicine has caused growing concerns about potential nanomaterial hazards to human health and the environment. Nanoparticles are particularly worrisome because their small size and large surface area alter their biodistribution and bioreactivity. Nanomaterials can infiltrate to the body via skin, respiratory tract, gastrointestinal tract, or direct injection (1). Airborne nanoparticles such as asbestos fibers, smoke, combustion, and other ultrafine particulate matter cause toxicity via pulmonary inflammation, oxidative stress, fibrosis, mutagenesis and cancer (2-5).

According to the National Cancer Institute, in 2015 in the US, lung cancer, breast cancer and prostate cancer have the 3 highest estimated numbers of new cases of all cancers (> 220,000, 13.3% of all cancers), and the estimated deaths cases because of lung cancer is the highest among all cancers (~ 160,000 cases, 26.8% of all cancers) (6). Although about 90% of lung cancer cases are related to smoking, data collected by the American Cancer Society from 1982 to 1998 over 500,000 adults from 51 districts nationwide showed that each elevation of 10 μg of fine particulate air pollutant was associated with ~ 8% increased risk of lung cancer mortality, whereas NO_2 , O_3 , CO levels didn't show such consistent association (7).

Despite the strong associations between particulate matter and lung diseases, the biological mechanisms are still being elucidated (3, 5, 8-13). Lung particulate matter toxicity depends on various factors including shape, size, solubility, surface area and

chemical components, and the physicochemical interaction of the particle surface (10). The toxicity mechanisms of these particles therefore are diverse and complicated. Donaldson and colleagues proposed that carbon nanotubes with high aspect ratios such as asbestos fibers can penetrate deeply due to their thin width, but they are not completely enclosed by macrophages due to their length, leading to phagocytosis frustration and failed clearance. The carbon nanotubes therefore will be accumulated in the lungs and cause inflammation (9). Many studies suggested generation of reactive oxygen species initiates toxicity, especially from metal or metal oxide nanoparticles (3, 10-13). For instance, Schins and colleagues' review on the inhaled particle toxicity to the lungs suggested the particles themselves could directly generate reactive oxygen species (ROS) or/and they can stimulate the ROS generation by target cells (primary) or by inflammatory cells (secondary). The ROS in turn can cause DNA damage and genotoxicity (3). Xing and colleagues also proposed three mechanisms of CuO and ZnO nanoparticle toxicity: oxidative stress, coordination effects and non-homeostasis effects. In the oxidative stress mechanism, the nanoparticles can generate ROS when they are in contact with oxidative organelles like mitochondria or in acidic surrounding as in lysosome. The excessively produced ROS disturbs the reactive oxygen production and damages DNA. With the coordination effects, the dissolved Cu and Zn ions from nanoparticles can bind to proteins, replace the important coordination atoms at the binding sites of the proteins and cause major structural changes such as unfolding, resulting in the inactivation of the protein function. Lastly, the appearance of extra metal

ions from the oxide nanoparticles in excess of physiological tolerance is toxic because it disrupts metal cation homeostasis in cells (10).

Although there have been several studies to elucidate the mechanisms and evaluate toxicity, most of them are done *in vitro*, require high dose of toxins, and cannot be observed in real time. In the next section a summary of some conventional assays for toxicity evaluation will be presented, following by the *in vivo* cytomagnetometry approach developed by Möller, Nemoto and others to study toxicity that can be carried on in a live, dynamic environment and with low dose of toxins.

Live/Dead Assays and Cytomagnetometry Approach to Study Cytotoxicity

Cytotoxicity measurements are commonly based on live/dead assays (or viability assays) such as the dye exclusion assays (trypan blue or propidium iodine staining), lactase dehydrogenase (LDH) leakage, MTT, or ATP. In these assays, live and dead cells are distinguished either by staining dead cells (trypan blue, propidium iodine) or by the identification and measurement of a specific molecule, generated when cells are dead (LDH) or alive (MTT, ATP assays).

More specifically, the principle of dye exclusion test is that live cell membrane is intact so that dyes such as trypan blue or propidium iodide cannot enter the cytoplasm to stain the intracellular compartments when cells are alive. However, these dyes can penetrate through the non-intact dead cell membrane and stain the cell in blue with trypan (14, 15) or bind to cell's DNA, RNA emitting enhanced red fluorescence with propidium

iodide (16). Similarly, in the LDH leakage assay, the amount of LDH outside of cells is an indicator of cell death because LDH is an intracellular enzyme that is released when cells are damaged or injured, measured by its activity on a protease substrate forming dye products that can be read by ELISA plate reader (17, 18). MTT or ATP, on the other hand, is based on live cell activity. MTT (3-(4,5-Dimethyl-2-thiazolyl)-2,5-diphenyltetrazolium bromide) or MTS (3-(4,5-Dimethyl-2-thiazolyl)-5-(3-carboxymethoxyphenyl)-2-(4-sulfophenyl)-2H-tetrazolium) are tetrazolium salts that are reduced to formazan by dehydrogenase enzymes in mitochondria of live cells. After MTT or MTS is added to the cell sample, the purple color of the formed formazan can be quantified by a photospectrometer (19, 20). The ATP assay is based on the requirement for ATP in oxidizing luciferin using luciferase to form oxyluciferin that emits fluorescence. Measurement of fluorescence signal reflects ATP levels and hence the live cell amount (21).

Cytotoxicity studies based on live/dead assays will not be effective if the toxic agent is not concentrated enough to kill the cells. Although gene expression can be used to identify early steps in apoptosis, such studies cannot be performed *in situ*. Meanwhile, biophysical approaches can be used to dynamically study the toxicity in living cells or even *in vivo* (in human or animal). The cytomagnetometry method is one excellent example among biophysical approaches of which the development is briefly introduced below.

In 1973 Cohen developed the magnetopneumography (MPG) method to detect magnetic materials in human body that may enter stomach from food cans or lungs from

welding. He first applied a strong external magnetic field to magnetize the unintentional ingested/inhaled magnetic particles for a short time and then measure the RMF generated by these particles in a shielded room. The measurable RMF suggested the MPG method could be applied in toxicity study in two different aspects: detecting asbestos (toxic and ferromagnetic) in the lungs of asbestos workers and determining lung condition with Fe_3O_4 particles (non-toxic and ferromagnetic) as tracers (22). In 1979 Cohen continued to use MPG to compare the clearance time of volunteer-inhaled Fe_3O_4 tracers from smoker and non-smoker lungs. His results showed 50% of the dust retained in the lungs of smokers after a year while in the non-smokers it was only 10%, indicating the smokers had impaired clearance (23).

Following these directions, several researchers including Nemoto, Valberg, Freedman and Möller have applied MPG to evaluate lung particulate matter toxicity both *in vitro* and *in vivo* and at the same time characterize some important properties of intracellular process. For instance, Freedman measured the ferromagnetic materials in the lungs of different occupations such as welders, miners and asbestos workers (24). Nemoto and Valberg estimated the viscosity and elasticity of the cytoplasm, and also the randomization energy caused by macrophages using simple models (25, 26). One notable conclusion from Nemoto study (25) was that the randomization of the particles' alignment was due to intracellular process in macrophages, not likely caused by the free diffusive Brownian rotation because the randomization energy was about 1000 times greater than the free energy (kT) of Brownian motion. In 1993, Möller and Stahlhofen also estimated the amount of dust in the lungs of dental technicians and welders and

found levels of 22 and 500 mg, respectively, compared to only 0.3 mg in control subjects. With the application of secondary magnetization, they determined the cellular energy, intracellular viscosity and the half time clearance (110 days) (27).

In 1997, Möller used phagocytized micrometer-size ferromagnetic tracers as a tool to non-invasively induce intracellular mechanical stress and observed the living-cell response. After the first short pulse (30 ms) of high magnetic field (100 mT) application and subsequent relaxation (2 – 5 min), a secondary magnetization was applied for about 10 s with a low magnetic field strength (0.2 – 3 mT) in the reverse direction to cause particle twisting. The RMF again was measured from which intracellular mechanical properties such as viscosity; elastic recoil and plasticity can be calculated. Their observation that the viscosity increased when the mechanical stress increased is typical for polymer solutions, indicating intact cytoskeletal networks in living cells. They suggested the elasticity was mainly related to the dynamic rearrangement of microfilaments. This study opened the door to investigate cellular dysfunction and drug administration (non-invasive intracellular torque generation) (28).

The examples above are studies that evaluated the condition of lungs or, on a more detailed scale, lung macrophages, using ferromagnetic tracers and the MPG method. The same principle can be applied to study particulate matter toxicity if the tracers themselves are the toxic particulate matter, such as asbestos. Even when the toxic matters and the tracers are not the same, researchers can study toxicity by observing tracers in the presence of toxins. In collaborative study by Möller and Nemoto, an adapted MPG method was developed, called cytomagnetometry, to study *in vitro* and in

real time the influence of cytoskeletal drugs on phagosome motion (29). This work was followed by cytotoxicity studies of ultrafine (nanometer range) particles that cause macrophage cytoskeletal dysfunction (30). In this cytomagnetometry method (29), the basis and experimental conditions were the same as summarized above from (28), with modifications for an *in vitro* instead of *in vivo* study. Cytochalasin D (CyD), colchicine (CoL) and acrylamide (AcL), the cytoskeletal drugs of microfilaments, microtubules and intermediate filaments respectively, were used to investigate their influence on phagosome transport. The disintegration of intermediate filaments by AcL affected neither stochastic nor directed phagosome movement. Microfilament disruption by CyD caused a slowdown of the random motion (or the relaxation after magnetization) and a small increase in cell stiffness. CoL depolymerization of microtubules reduced viscous resistance and elasticity. The results implied that microfilaments were important in the stochastic transport of phagosome whereas microtubules were essential for the static mechanical properties of the cell (29).

In 2002, Möller and colleagues applied a cytomagnetometry method (called magnetic twisting cytometry – MTC in subsequent studies) to evaluate the cytotoxicity of ultrafine particles (UFP) including TiO₂, elemental carbon, commercial carbon black, diesel exhaust particulate matter, and urban dust. The results showed cytotoxicity effects, such as impairing phagosome transport and increasing cell stiffness, of all UFP types at concentrations from 100 ug per mL per 10⁶ cells, except for TiO₂; and the urban dust and diesel exhaust particles were found to cause cytoskeletal dysfunctions as much as elemental carbon (30). This research work is a representative example of using

ferromagnetic tracers and cytomagnetometry technique to study the cytotoxicity of nano-size materials that we want to apply in our research work to study lung particle toxicity.

Although MTC is a useful method to study lung particle toxicity, it does not show individual tracer behavior and therefore misses reporting the regional properties. We have modified the cytotoxicity experimental methods using MTC to implement a single particle tracking technique that will be introduced in the following section. In our approach, ferromagnetic tracers are replaced by anisotropic optical tracers that have orientation-dependent optical properties (these tracers can be magnetic or not, depending on the experiment) and the magnetic sensing system of MTC is replaced by a light microscope. Although our current method is *in vitro* with cultured macrophages only, the *in vivo* study of human lungs could be achieved with an endoscope.

Single Particle Tracking, SPORT, and Our Approach to Study Cytotoxicity with Anisotropic Optical Tracer Tracking

As previously mentioned, our approach to study cytotoxicity is the combination of modified MTC to apply for optical system with single particle tracking technique but before explaining in more detail the method single particle tracking (SPT) will first be introduced.

SPT uses a microscope and integrated camera to record hundreds to thousands or more images over time (time-lapse microscopy) of multiple individual micrometer- or nanometer-size tracers (organic dyes, fluorescent dyes or proteins, or particles such as

quantum dots or gold nanoparticles) (31) in order to obtain dynamic information about the tracers' surroundings or the organelles the tracers are associated with. Tracers' brighter signal (intensity) over the background of the image is the key point of the algorithms to identify and extract their trajectories. Data analysis with the help of computational tools to characterize the tracers' movement reveals insights into the properties or mechanisms of the studied system.

SPT is commonly used to study dynamic cell-related biophysical processes where it is referred as live-cell SPT. Live-cell SPT of a population of tracers over different regions in cells will provide not only the average properties of the whole population but also the local information from each individual particle in that population. Information such as forces that drive a particular particle motion and rate of movement can be obtained (32). The main advantage of using SPT to study biophysical processes is that it helps resolve different subpopulations in their dynamic states.

An early application of SPT was to identify kinesins' role in the movement of plastic beads along microtubules from squid axons *in vitro* (33, 34). Since then SPT has been utilized to study various biophysical processes including but not limited to extracellular, intracellular (in particular intracellular transport) and cellular membrane dynamics, as being described and reviewed in (35-39). For example, Selvin and Yildiz used the Fluorescence Imaging with One Nanometer Accuracy (FIONA) technique to characterize the movement of the three molecular motors myosin V, myosin VI and kinesin with 1 nm accuracy. FIONA precisely determined the center of a fluorescent spot by fitting the spot's point spread function with a two-dimensional Gaussian function.

Collecting more photons and reducing background also improved the precision. For molecular motor movement study, both the head and the level arm of the motors were labeled with an organic dye and the dyes were tracked during motion. Their results showed that all the three type of molecular motors walked in a hand-over-hand manner (35). Cappello and colleagues first used quantum dots (QDs) –much brighter tracers than normal dyes – in intracellular tracking to characterize kinesin movement in live HeLa cells. They tagged kinesin with a single QD, tracked and computed the mean square displacement (MSD) in order to characterize motions. Of the 75 QDs (radius ~ 15 nm), they identified approximately 13% had directed motion, and the remaining had random motion with a diffusion coefficient of $0.031 \pm 0.002 \mu\text{m}^2/\text{s}$ (36). The 18 nm super-bright and photo-stable fluorescent probes formed by precipitation of highly fluorescent conjugated polymers were also used, with extremely low concentration of hundreds pM range, in cellular uptake mechanism study (40). Recent reviews indicate SPT is a powerful technique in drug and gene delivery research that aids in unraveling cell entry mechanisms of viruses and pharmaceutical nanoparticles (41-43).

Tracking requires accuracy to properly evaluate the investigated moving system.

The resolution of SPT depends on factors listed in the equation below:

$$\langle \Delta x^2 \rangle = \frac{s^2}{N} + \frac{a^2}{12N} + \frac{8\pi s^4 B^2}{a^2 N^2}, \text{ (Equation 1)}$$

where

Δx is the error in the particle position

s is the standard deviation of the point spread function

N is the number of photons detected

a is the pixel size

B is the background noise

This equation will be used to estimate the resolution of our tracking.

Although SPT is a powerful tool to study real time in live cells and provides regional information from each individual tracer, translational tracking (tracking based only on the displacement in X and Y coordinates) has difficulties in a moving system and at low magnifications as in endoscopes. Meanwhile, rotational motion, if it can be tracked, is not altered by small changes in the studied objects' position.

There have been different approaches for rotational tracking as reviewed in (44). The Selvin group developed a technique called defocused orientation and position imaging (DOPI) by combining the FIONA to identify the position and defocusing the object (QD rod) to determine its orientation, because defocused image has lobes and fringes representing orientation that can be classified by comparing to respective simulations. Using this technique, Selvin and colleagues were able to confirm the 37 nm step size of myosin (45). Ning Fang and colleagues have used differential interference contrast (DIC) microscopy to develop the DIC-based single particle orientation rotational tracking (DIC-based SPORT) for rotational tracking of plasmonic nanorods. The key points of this technique are an anisotropic optical tracer (nanorod) and the DIC microscopy capable of identifying the tracer orientation based on its intensity. The basis of DIC is summarized as following. A polarizer is used to polarize the illumination beam. A first Normarski prism is then placed to split the polarized illumination beam into two

beams that are orthogonal and shifted by a sub-wavelength shear distance, resulting in two intermediate bright-field images that are later shifted back by a second Normarski prism as well as being projected to the same polarization plane by a second polarizer. This creates an interference image with bright and dark areas, corresponding to constructive or destructive interference depending on the specimen thickness and/or refractive index. This method was used to study intracellular transport by motor proteins both on engineered surface and in live cells (46). Working well for rotational tracking but the localization of a particle determined by conventional DIC has limitation because of the disproportionate bright and dark parts. A later publication from the same group described the implement of superlocalization with DIC for tracking both translation and rotation. Herein, a dual-modality was applied where a dichroic mirror is placed after the second prism and before the second polarizer of the DIC setup to create two channels, one follows the path as in a normal DIC system as described above to give rotational information and the other doesn't have a polarizer, and produces a normal bright-field image used for translational tracking. This method was applied to track endocytosed gold nanorods in live cells with nanometer-scale localization precision (47). Applying the same principles with the described dual-modality, this group showed the tracer's position in correlation with the microtubule it was on by combining DIC with fluorescence (48).

In a simpler system with fluorescence or dark-field light microscopy, rotational and translational tracking can also be obtained by measuring the fluorescent or scattering intensity of optically asymmetric particles when they rotate (49-51). In place of the nanorods as in the Fang group experiments, tracers can be micro/nano-spheres, fabricated

by vapor depositing a thin layer of metal (gold, silver, or aluminum) on to one hemisphere so that the tracers will have orientation-dependent fluorescence or scattering. This causes the change in intensity when tracers rotate as they move. The motion of these anisotropic optical tracers in time is observed by a microscope and recorded by a camera. If the tracers are magnetic, they could serve as multi-purpose probes to study intracellular processes, to generate intracellular mechanical force, or to control local drugs delivery to cells.

In our approach to study biophysical processes by tracking anisotropic optical tracers in real time, we want to combine Möller approach to study cytotoxicity with the advantages of SPT to add the benefits from the ensemble of multiple particles for both local and global, both translation and rotation information. We fabricated anisotropic optical tracers (MOONs or MagMOONs) from spherical probes by vapor deposition one side of these probes with a thin metal layer. This metal layer limited light penetration, causing different optical property compared to the non-coated side. We take from Möller's studies the idea of using tracers to study toxicity, but we innovate the idea of tracking these tracers individually. From the viewpoint of rotational and translational tracking, the novelty is applying the technique to study toxicity. Our approach is expected to detect toxicity effects at low doses that cause slight inflammation or cytoskeletal impairment before the effect becomes so serious that it kills cells.

In summary, tracking rotation and translation of anisotropic optical tracers is potentially a novel toxicity assay that optically measures intracellular transport and can be done *in situ*. Single particle studies will reveal information about the mechanism of

cytoskeletal impairment that is comparable to conventional techniques, especially the magnetometry MTC method reported by Möller and others, and at the same time gaining more detailed information of toxin effect on macrophage phagocytosis and transport. Our approach will be a complementary tool to conventional cytotoxicity assays.

CHAPTER TWO

TRACKING MAGMOONS TO DETECT GELATION AND DE-GELATION

Before going into the details of our intracellular transport and cytotoxicity study in Chapter Three, this chapter will present the application of anisotropic optical tracers to *in situ* detect through tissue the chemically induced de-gelation process of alginate gel. This is a demonstration to show proof-of-principle for detection of bacterial biofilm formation on medical implants by sensing specific proteases that either activate a related function or regulate biofilm formation. It can also be applied to other biosensors and drug delivery systems based on enzyme-catalyzed breakdown of gel components.

Introduction

Alginate gels and their derivatives are widely used for implanted devices and drug delivery (52, 53). These gels can serve as a local source of proteins, nucleic acids, and small molecule drugs; and gel degradation will release these molecules (54-58). The gels are also used in wound dressings and as a platform for cell cultures (59, 60). They are increasingly used in tissue regeneration by carrying and delivering proteins and cells that promote bone, muscle, cartilage and blood vessel formation (61-64).

In general, a gel allows small molecules and particles to diffuse through it, but effectively prevents the motion of particles that are large compared to the gel network mesh size. The gel can be dissolved by either breaking the crosslinks in the gel network,

or enzymatically cleaving the polymer backbones, allowing rapid drug release. After the gel breaks down, larger probes become free to move, and the effective viscosity dramatically decreases. Detecting this rapid change in viscosity during de-gelation can also be used to determine the activity of enzymes that digest the gel. *In vitro* viscosity can be measured using standard viscometers such as capillary (65), plate, or falling-ball viscometers (66). To measure local viscosity in confined systems such as a cellular cytoplasm or measurement through tissue, more sophisticated methods are needed to move a probe and measure its response. Möller and colleagues measured the local viscoelastic moduli of the macrophages cytoplasm by recording the deflection and recovery of 1.3 μm magnetic beads when applying twisting force pulses (67). They also studied the intracellular phagosome transport in macrophages by monitoring the RMF of $\sim 10^6$ phagocytized magnetic particles after initially magnetizing them with a strong magnetic field. The RMF decayed as each particle rotated away from its initial orientation by independent intracellular transport forces in each cell (29, 68). This is an excellent non-invasive approach for intracellular investigation. However, they required $\sim 10^6$ particles to measure the RMF and this approach cannot take advantage of SPT to obtain local information of the surrounding of each individual particle using this method.

In addition to magnetometry approaches, mechanical methods based on oscillation or vibration of a cantilever have also been developed (69-71). For example, Ehrlich and co-workers designed a wireless biosensor device for early biofilm detection based on changes in the resonance frequency of a cantilever in response to change in viscosity as a polysaccharide gel was cleaved by its enzyme galactosidase (69). This

galactosidase enzyme was designed to activate upon binding of RAP (ribonucleic acid [RNA] III activating protein), a quorum-sensing molecule generated by bacteria. When activated by RAP, the enzyme cleaved a polysaccharide substrate and produced glucose, which broke down a dextran-Concanavalin A hydrogel by competing with the dextran for binding to the concanavalin A crosslinks. This RAP-activated gel breakdown reduced the hydrogel viscosity and was detected as an increase in the cantilever's amplitude and resonance frequency due to reduced viscous damping. This approach is sensitive but requires a power source, relatively large and complex electronics, and antenna to drive the cantilever circuit and transmit the signal wirelessly.

Inspired by Ehrlich's work, we aimed to create a simple yet effective fluorescence-based sensor to detect changes in viscosity due to de-gelation activity, and monitor the fluorescence through tissue. In place of piezoelectrically driven cantilevers, we applied an oscillating magnetic field to drive the rotation of MagMOONs embedded in the gel, and measured the ability of the MagMOONs to rotate and align with the field by detecting the modulated fluorescence signal. In general, the rotational motion of magnetic particles depends upon the applied magnetic field, the magnetic moment of the particle, shape and size-dependent drag, and the viscoelastic properties of the environment. For a given set of particles, the rotational motion can be used to monitor changes in the environment. If particles are optically asymmetric, the motion can be tracked optically on a single particle level (provided that the particles can be resolved, i.e., tissue does not scatter the light). For example, in 1950, Frances Crick monitored the rotational motion of micron-sized aspherical particles in response to pulsed magnetic

fields to measure the viscosity in chick fibroblasts (72). Optical tracking of rotating magnetic particles was used to monitor changes in drag during growth of single bacteria on MagMOONs (73) to monitor changes in shape of single cancer stem cells (74), to measure the viscosity of butterfly saliva (75), and to detect bacteria based on changes in viscosity when bacteria excrete biofilm polymers (76). In addition, particle rotation has been used to track intracellular transport (46, 49). McNaughton and colleagues used asynchronous magnetic bead rotation (AMBR)-based biosensor to measure viscosity and to detect microbial growth based upon increased drag on the magnetic particles. They applied a circularly rotating magnetic field that caused the particles to rotate at the driving frequency (with a phase delay) when the rotation was slow (and/or the field is strong), or in an asynchronous rocking motion superimposed with continuous rotation when the rotation exceeded a critical frequency ($\omega_c = mB/\kappa\eta V$), where B is the applied field, κ is a shape factor (6 for a sphere), η is the viscosity, and V is the particle volume. When the viscosity of the environment surrounding the bead changed or the effective volume changed (e.g., due to a bacterium binding onto the bead surface), the rotational period of the bead changed accordingly (76, 77). This method has high sensitivity at the single-bacterium level (74). However, the method does not work unless single particles can be resolved, since each particle rotates asynchronously and no large group of particles would be aligned with each other at any given time.

Although local viscosities can be probed by optically tracking the motion of magnetically driven particles *in vitro*, such tracking is challenging to perform through tissue for three reasons: first, the excitation light and probe fluorescence is attenuated by

the tissue; second, tissue autofluorescence can obscure the probe signal; third, tissue scattering can cause the image to blur, preventing accurate determination of the position of single particles. Fortunately, these limitations can be circumvented using MagMOONs. MagMOONs are fluorescent particles with an orientation-dependent fluorescence signal generated by vapor depositing metal onto one hemisphere of a fluorescent particle, and a magnetic moment that causes them to align in an external magnetic field, (see **Fig. 2.1** and methods section). The MagMOONs feel a torque to align with an external magnetic field. If the MagMOONs are free to rotate in an oscillating external magnetic field, they blink as they flip between dim and bright orientations. Tissue does indeed attenuate the MagMOON fluorescence signal, but acceptable signals can be obtained by choosing the proper wavelength of the fluorescence excitation and emission as well as adjusting particle concentration. In the current study, a 50 mW 514 nm Ar ion excitation laser was found to be sufficient to detect through 4 mm tissue thickness 400 μ L MagMOONs solution 1 to 2×10^4 particles/mL (ca. 50 to 100 ng/mL, formed ~ 800 μ m thick layer of solution between two 1 inch diameter coverslips). It is expected that larger depths will be attainable for higher concentrations of red or near-infrared exciting and emitting MagMOONs. The problem of autofluorescence can be overcome because only the probe signal is modulated by the external magnetic field. This allows measurements even when the background fluorescence is thousands of times more intense than the probes' fluorescence and changes in time due to photobleaching and physiological changes, as long as these changes occur at different frequencies from the MagMOON modulation. Ultimately, the signal-to-noise ratio is limited by noise on the

background at the driving frequency, including shot noise on the background fluorescence (78). Importantly, tissue scattering blurs the probe signal with a point-spread-function approximately equal to the tissue depth (79, 80) and also reduces the contrast between bright and dim MagMOON orientations as scattering scrambles the direction of excitation and emission light (81) Although this scattering prevents single particles from being resolved and tracked in tissue, we can still measure the intensity change from an ensemble of particles that are driven to rotate and blink together. The work described here used uniform magnetic fields and had poor spatial resolution, however, in principle it is possible to improve the resolution either through endoscopy, or by restricting the region of modulation using appropriately designed magnetic fields and scanning the field across the sample (e.g., the field orientation and strength changes the most in the null region between opposing field sources) (82, 83).

In this study, we developed a MagMOON-based sensor film to detect alginate lyase protease activity based on the release of MagMOONs trapped in an alginate gel. Alginate was selected as a model system because it is a natural polysaccharide widely used in biomedical applications, especially in drug delivery, due to its unique properties such as being biodegradable, injectable and chemically modifiable (53, 54). Monovalent alginate salts (Na^+ , K^+ , NH_4^+) are soluble in water while the divalent cations (Ca^{2+} , Ba^{2+} , Sr^{2+}) ionically link the alginate polymer chains together and cause gelation. Therefore, alginate gels are formed when transforming from the monovalent salt form to the divalent salt form, and the reverse reaction causes de-gelation. We used a calcium ion solution to induce gelation of an alginate and MagMOONs mixture. The resulting MagMOON-

trapped calcium alginate gel then was used as a sensor for detecting alginate lyase, the protease of alginate that cleaves the 1-4 O link between monomers of the alginate chain (84). As the bonds are cleaved, MagMOONs are released from the gel matrix and become free to rotate. Each individual MagMOON can be tracked based on its blinking signal under the magnetic modulation. Therefore, the activity of alginate lyase is indicated via MagMOONs blinking signal. The technique we use in this study can also be applied in other biosensors and drug delivery systems based on enzyme-catalyzed breakdown of gel components.

Method and Experimental Setup

The 4.8 μm fluorescent Nile Red carboxyl ferromagnetic particles were provided by Spherotech (Spherotech, Lake Forest, IL). The particles were comprised of a fluorescent polystyrene core and a shell containing ferromagnetic chromium dioxide nanorods. Modification of these particles into MagMOONs was described in previous papers (49, 50, 85, 86). Briefly, 15 μL of 4.8 μm ferromagnetic fluorescent particles 1% w/v dispersion in water was mixed with 240 μL ethanol using a vortex mixer, deposited evenly onto six 25 mm-coverslips, and allowed to dry. A layer of aluminum was deposited onto the coverslips using an Auto 306 (BOC Edward, West Sussex UK) thermal vapor deposition system. During this process, aluminum vapor from a heated tungsten boat travels ballistically through vacuum to coat the glass coverslips as well as the top hemisphere of the fluorescent particles on the coverslip. The thickness of the aluminum layer was measured during deposition using a 6 MHz quartz crystal

microbalance; deposition was stopped at 70 nm. The hemispherically coated MagMOONs were magnetized in a uniform field so that the magnetic moment of all MagMOONs pointed in the same direction (towards the coating); (**Fig. 2.1a-d**). The particles were then removed from the coverslip and suspended in alginate solution as described below.

An air core solenoid with 24 mm hole diameter, 35 mm height, and 210 turns of 26 gauge magnet wire served as an electromagnet generating a magnetic field of ~ 0.5 mT at the centre of the microscope stage when powered with 0.25 A and 1 V. To modulate the MagMOONs, it was programmed to switch the field from North-facing to South-facing every 5 s (for the gelation by calcium and de-gelation by ammonium) or 2 s (for all other experiments). This relatively long modulation time with the 0.5 mT applied field was used to provide enough time for all free particles to orient, especially to minimize read noise when extracting the modulated spectrum from the background. In the future we will design a system with photomultiplier tubes to collect light from a larger field of view than the microscope, which is expected to improve signal to noise ratios and allow more rapid detection with less read noise. **Fig. 2.1e** illustrates the working principle. In an oscillating external magnetic field, the MagMOONs appear to blink as they turn from a dim orientation, with the metal-coated side facing the objective, to the bright orientation, with the uncoated fluorescent side facing the objective. This blinking signal can be separated from un-modulated backgrounds by filtering the signal at the driving frequency (85). **Fig. 2.1g** shows an example of two single MagMOONs

rotating and blinking. About 30 s after adding CaCl₂ 0.1 M (75 s after the start of the experiment), the rotation stops as the gel forms.

Alginate lyase from *Sphingobacterium multivorum*, powder, >10,000 units/g solid was purchased from Sigma Aldrich (Sigma Aldrich, St. Louis, MO) and freshly made into 4 mg/mL solution in distilled water. NH₄Cl and CaCl₂ were purchased from Acros Organics (Acros Organics, Morris Plains, NJ) and were made into 2 M and 0.2 M solution, respectively. Sodium alginate was purchased from Alfa Aesar (Ward Hill, MA) and was freshly dissolved in distilled water to make a 10 mg/mL solution. This solution (20 μL) was pipetted on a coverslip with freshly prepared MagMOONs after coating via aluminum vapor deposition and magnetizing (see previous paragraph). The area in the drop was scraped either with a pipette tip following by pipetting the MagMOONs-alginate mixture and disperse in sodium alginate 10 mg/mL with the ratio of 70 μL sodium alginate 10 mg/mL per coverslip, or a camel hair #0 paintbrush following by sonication of the paintbrush in sodium alginate. The MagMOON-sodium alginate mixture (10 μL) was then spread onto a 25 mm-coverslip that was previously cleaned by plasma-etching with a Harrick plasma cleaner (Harrick Plasma, Ithaca, NY) and 20 μL CaCl₂ 0.2 M was dropped on top of the mixture to form a ~ 100 μm thick calcium alginate gel with MagMOONs. The gel was left for 5 minutes before gently washing with distilled water. The coverslip was then left to dry under ambient conditions for 30 minutes before imaging. The particle concentration in the formed gel was estimated to be ~ 5 x 10⁴ particles/mL. To determine whether the MagMOON concentration within the film was uniform, we counted the number of particles in several images of a thin film gel

made between two cover slips (0.35 mm in thickness and 15 mm in diameter). We examined 36 fields of view ($690 \mu\text{m} \times 517 \mu\text{m}$) and counted 63 ± 17 particles per field view. The standard deviation is approximately twice what we expected from Poisson statistics, indicating that although the distribution appears random within an image, there is some heterogeneity in concentration across the film. **Fig. 2.1h** shows a representative image of particle distribution in a field view.

Fig. 2.1f is a schematic of the microscope setup. A Leica DMI5000 epi-fluorescence microscope (Leica Microsystems, Bannockburn IL) with a 10x, 0.3 NA objective lens was used for all experiments. For SPT experiments, the sample was illuminated using blue light excitation from a filtered mercury lamp and images were continuously acquired every 1 second (0.2 s exposure time) using ORCA-Flash 2.8 CMOS camera and HCSImage software (Hamamatsu, Bridgewater, NJ). The fluorescent intensity was exported and analyzed using a SPT script in Matlab program. For measurements through tissue, a 50 mW Ar-ion 514 nm laser was used as the excitation source. The emission signal was collected in an epi-fluorescence configuration using DNS 300 spectrometer (DeltaNu, Laramie, WY) equipped with an Andor DU420A-BV CCD camera and Andor software (Andor Technology, South Windsor CT) with an acquisition time of 0.2 s per spectrum.

For SPT, custom Matlab scripts were written to extract from the acquired fluorescence movies the position and fluorescence intensity of single particles in time (Appendix C). The particle position was determined from the intensity centroid within a region around the particle, after applying a threshold to remove background signals. The

total intensity of the tracked region was also recorded. Although all particles in view could be tracked simultaneously, to ensure comparable data, we selected for tracking only particles that were well separated (more than 2 particle diameters), and stayed in the field view and within a certain range of focus. In addition, we removed a few rare particles that didn't blink (either because they were uncoated or stuck to the glass), or had paths that crossed each other. Using these selection criteria, on average ~ 50% of the particles in view were trackable.

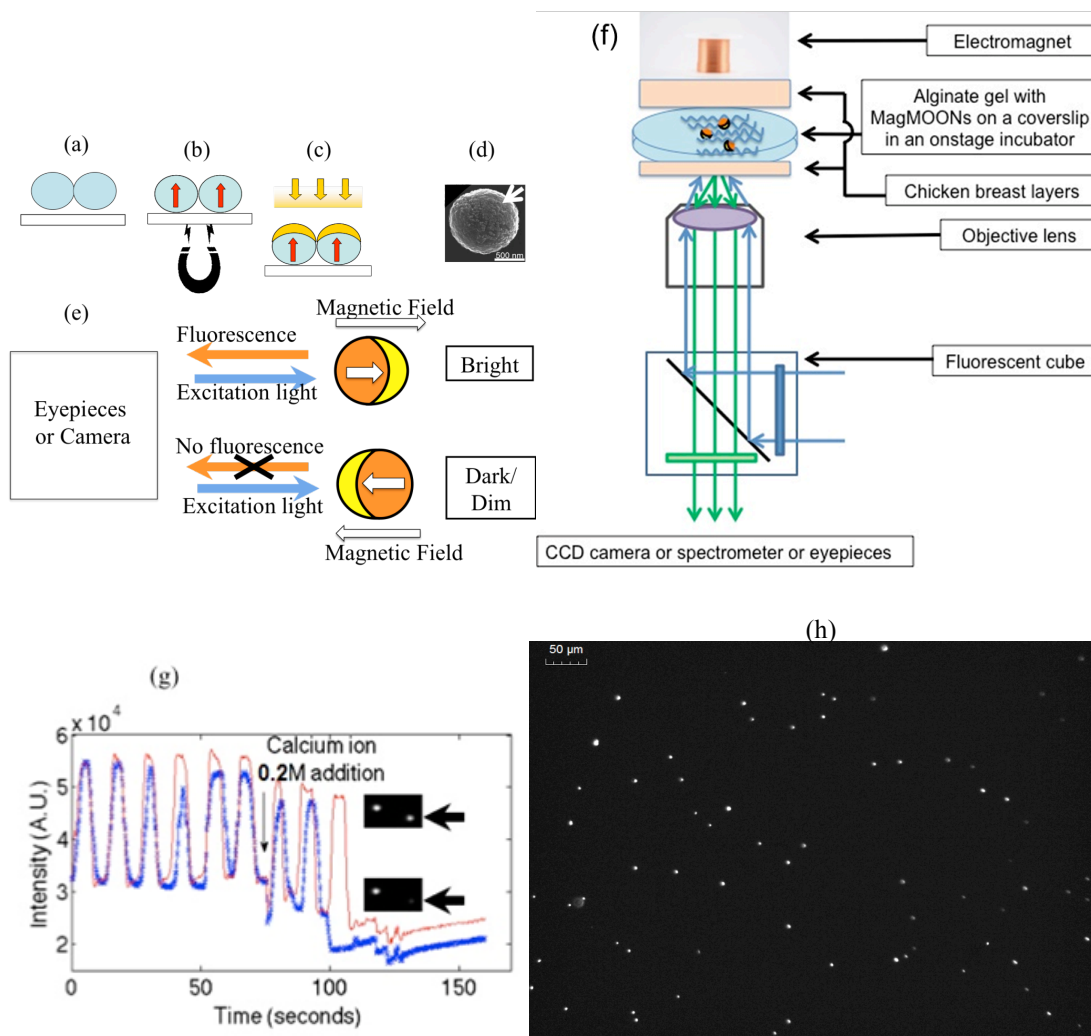


Fig. 2.1. Experimental setup. (a)-(d) Fabrication process: (a) $4.8\ \mu\text{m}$ fluorescent ferromagnetic microspheres deposited on a glass coverslip. (b) Microspheres magnetization. (c) Metal (Al, Au, or Ag) vapor deposited onto one hemisphere of the microspheres. (d) SEM image of a Fe_3O_4 MagMOON. The arrow points to the Au-coated side. (e) Working principle: MagMOONs blink when they rotate in response to rotating magnetic field. (f) Schematic of fluorescence microscopy setup. (g) Two single MagMOONs blinking before and after $0.2\ \text{M}$ CaCl_2 addition to $10\ \text{mg/mL}$ alginate (at $\sim 75\ \text{s}$). Insets show one frame where both MagMOONs are bright, and one frame where one MagMOON is trapped in the dim orientation. (h) Representative fluorescence image of MagMOONs in a gel for determining particle distribution.

For experiments performed through tissue, we collected the fluorescence spectra as a function of time during modulation. We then calculated the average intensity from 544 nm to 867 nm (just past the long-pass emission filter to the last pixel in the spectrum) in order to increase the signal to noise ratio for studying the blinking waveform over time.

For the experiment on de-gelation by NH_4Cl , the prepared coverslip with MagMOONs-trapped calcium alginate gel was put in an open on-stage chamber. Distilled water (400 μL) was added to the chamber, forming a ~ 1 mm thick water layer above the gel. During the acquisition, an additional 400 μL NH_4Cl 2 M was added by pipette to cause de-gelation.

For the experiment on de-gelation by alginate lyase, the prepared coverslip with MagMOONs calcium alginate gel was pre-incubated in 400 μL distilled water at 37 $^\circ\text{C}$ for 10 min. During the acquisition, 400 μL alginate lyase 4 mg/mL was added to cleave the calcium alginate matrix.

To detect the effect of alginate lyase on calcium alginate matrix through tissue, the prepared calcium alginate thin film coverslip was placed in a chamber embedded with square slices of chicken breast (Tyson Foods Inc., Springdale AR), 2.5 x 2.5 inches, wrapped in clear plastic. The top chicken slice was about 1 cm thick while the bottom slice was varied from 1 mm to 6 mm. In the control test alginate lyase was denatured by boiling for 30 minutes. The alginate lyase was added right before placing the top tissue slice and starting the acquisition.

Results and Discussion

To induce de-gelation of the calcium alginate gel, we used two approaches, as shown in **Fig. 2.2**. First, we added ammonium ions to the gel to compete with and replace the cross-linked calcium ions in the calcium alginate gel. Second, we applied alginate lyase to the gel to cleave the glycosidic 1 → 4 O-linkage between monomers of the alginate chain and cause gel destruction. In both cases, initially trapped MagMOONs became free to rotate and blink along with the external magnetic field. We could effectively monitor the de-gelation process by tracking the position of single MagMOONs or the total intensity change under magnetic modulation.

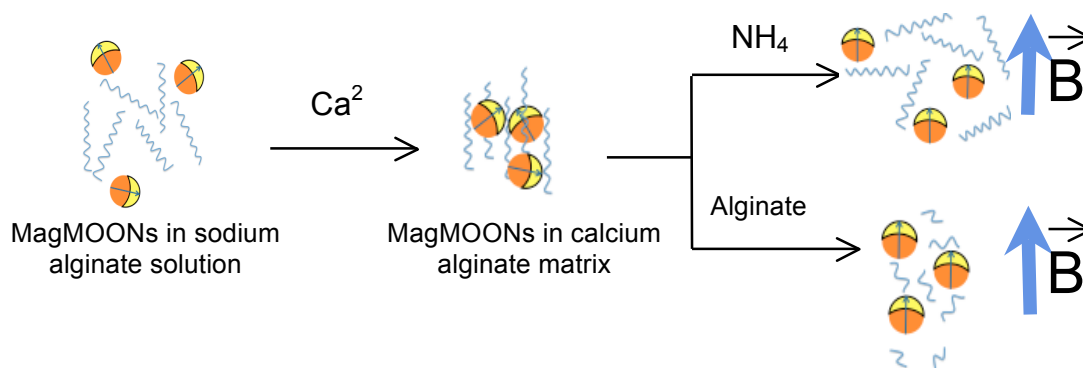


Fig. 2.2. Summary of gelation and de-gelation experiments.

We also demonstrated the ability to track through tissue the modulated fluorescence intensity from an ensemble of MagMOONs. The calcium alginate gel with entrapped MagMOONs was placed between two slices of chicken breast and a 514 nm laser excited the fluorescent signal from MagMOONs. The modulated signal decreased

dramatically with the increase of tissue thickness but was clearly identified through up to 4 mm tissue.

Monitoring de-gelation by tracking individual MagMOON motion

Alginate includes mixed polymer chains of different arrangements of α -L-guluronate (G), and β -D-mannuronate (M) monomers. In sodium alginate, $-\text{COOH}$ groups are partly replaced by $-\text{COONa}$ (87, 88). Alginate gels form in the presence of divalent ions such as Ca^{2+} and dissolve when monovalent ions such as NH_4^+ displace the divalent ions. The calcium alginate gel structure is maintained by the coordination of Ca^{2+} with oxygen atoms in a cavity created by a pair of guluronate sequences along alginate chains. According to the literature, during gelation, egg-box like dimers form first and then laterally associate to form egg-box multimers (89). Unlike divalent cations, monovalent ions such as Na^+ , K^+ , Li^+ or NH_4^+ cannot serve as crosslinkers between guluronate sequences, hence the displacement of Ca^{2+} ions by NH_4^+ ions destroys the gels.

In our experiments, we tracked the position and intensity of MagMOONs in a calcium alginate gel as a function of time during de-gelation. To destroy the gel structure and cause de-gelation, we added NH_4Cl 1 M to calcium alginate gel to replace Ca^{2+} ions. **Fig. 2.3a** shows the background-corrected fluorescent intensity as well as x- and y-displacements of a representative MagMOON. At the beginning when the MagMOON was fixed in the gel, its intensity remained unchanged with time because the gel prevented it from rotating. After about 4 minutes, enough ion replacement had occurred to release the MagMOONs from the matrix and the MagMOON fluorescence began to

blink in response to the oscillating magnetic field. During the de-gelation process, the amplitude of the modulation increased, presumably due to the gradually release of MagMOON from the matrix as the polymers were cleaved. We used a low magnification objective to observe many particles simultaneously, which made it difficult to accurately discern the shape of the fluorescent crescent as the MagMOON rotated. However, the shape could be discerned well enough to determine that after ~ 320 s, the MagMOON was almost fully modulated (fully bright to fully dim).

To compare the de-gelation behavior of multiple particles with different volumes and fluorescence intensities, we defined the “de-gel time” as the point when the modulated amplitude reached 20% the maximum amplitude. We removed from analysis particles that clearly moved out of focus before fully modulating. The de-gel time of the MagMOON in **Fig. 2.3a** was determined to be ~ 300 s, as measured from its short-time Fourier transform spectrogram (**Fig. 2.3c, d**). **Fig. 2.3b** shows the position tracks of four individual MagMOONs in the observation view (including the representative one in **Fig. 2.3a**). The initial position is marked with a black star, and the position at the de-gel time is marked with a colored dot (with the color indicating the de-gel time). Plotting the displacements and de-gel time together revealed interesting information about the heterogeneity of the de-gel process. First, it is clear that the particles followed almost the same path, indicating that the entire gel flowed together in this region. Second, there was significant heterogeneity in de-gel time, with one of the four particles (yellow spot) taking twice as long to blink as the other three and moving about $20 \mu\text{m}$ before it blinked.

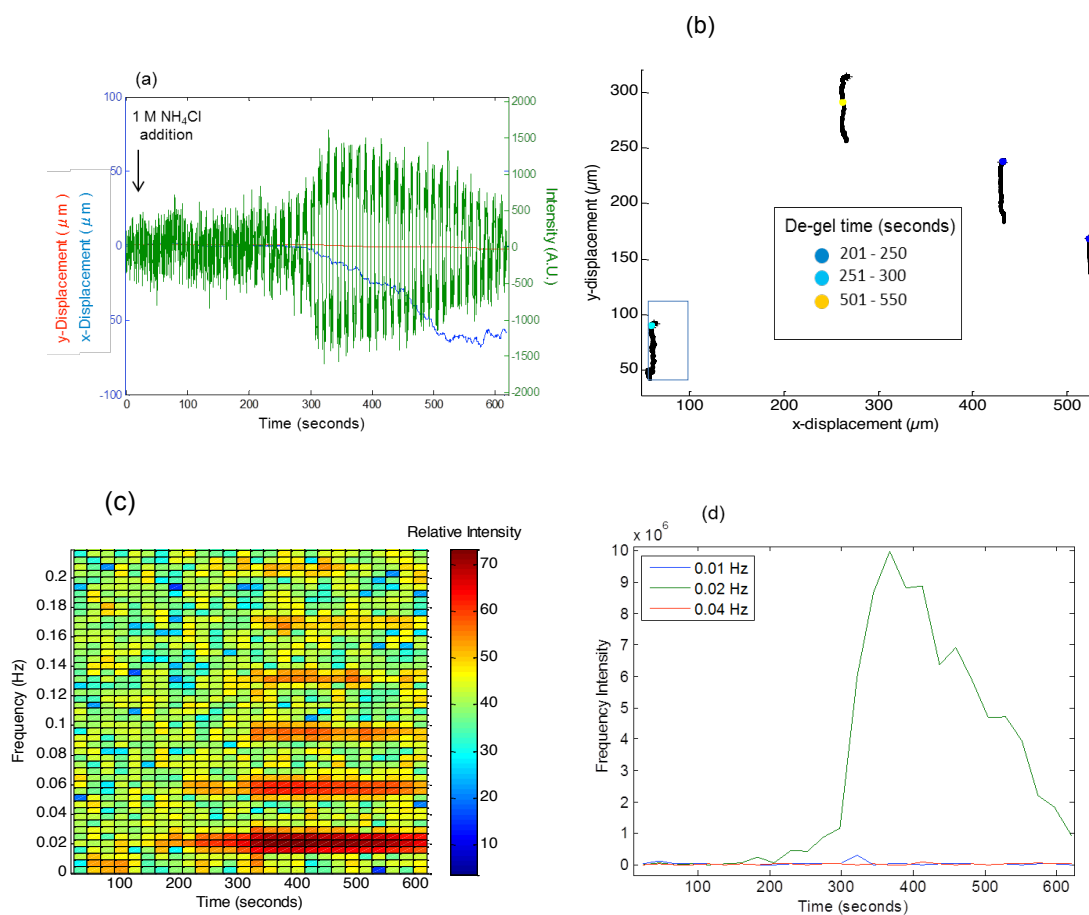


Fig. 2.3. Tracking individual MagMOONs to detect alginate de-gelation by ammonium ion replacement. Intensity and x, y-displacements of one representative MagMOON are plotted in (a): x-displacement (blue line, left y-axis), y-displacement (red line, left y-axis) and fluorescence intensity (green line, right axis). Modulation is seen after about 300 s. (b) The plot of de-gel time (color-coded spots) with x, y-displacements for single MagMOONs to show different MagMOONs in the same field view de-gelled at different time. The MagMOONs plotted in (a) are marked in blue boxes in (b). Black stars (*) indicate the initial MagMOON position. The short-time Fourier transform (27 windows, each 23 s long) spectrogram shows MagMOON modulation after ammonium addition: (c) Spectrogram of relative Fourier component amplitude (log scale, color-coded) as a function of frequency and time. (d) Plot of Fourier component amplitude in time at the driving frequency (0.02 Hz) and two other non-modulating frequencies.

Having successfully tracked MagMOONs during de-gelation by ammonium ions, we next used the MagMOON-trapped calcium alginate gel to detect de-gelation from alginate lyase activity. Alginate lyase catalyzes alginate degradation by cleaving the 1-4 O linkage between monomers (84). As the chains are cleaved, MagMOONs are released and become free to rotate with the magnetic field. We pre-incubated the prepared MagMOON-calcium alginate gel coverslip in 400 μ L distilled water at 37 $^{\circ}$ C for 10 minutes before acquisition. During the acquisition, 400 μ L alginate lyase (4 mg/mL) was added to cleave the calcium alginate matrix. **Fig. 2.4a** shows the x, y-position and background-corrected intensity of a representative MagMOON immediately following 2 mg/mL alginate lyase addition. The MagMOON started to move laterally after around 350 s, as indicated by the increasing slope of x and y-displacements; however this lateral motion was not yet accompanied by fluorescence blinking. After \sim 600 s the MagMOON began blinking while simultaneously moving. In this case, plotting the intensity change together with the x and y-displacements elucidates the 2 steps (lateral moving without blinking first and then moving with blinking) of the de-gelation process observed. The motion during both steps was directed rather than diffusive, suggesting that as the alginate gel disintegrated, convection currents were generated before particles were released and able to rotate and blink. By tracking modulation of the MagMOON intensity, MagMOON rotation was detected independently from this convective transport.

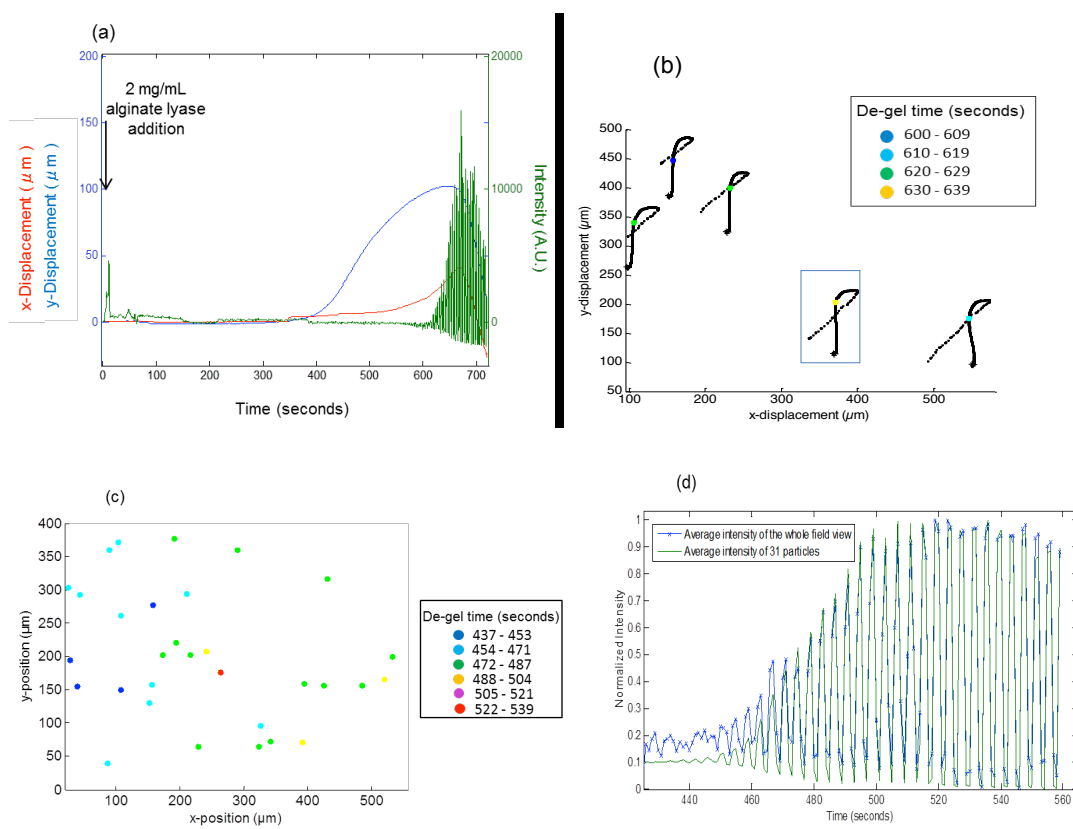


Fig. 2.4. Tracking individual MagMOONs to detect alginate de-gelation by alginate lyase. Intensity and x, y-displacements of one representative MagMOON are plotted in (a) - alginate lyase: x-displacement (blue line, left y-axis), y-displacement (red line, left y-axis) and fluorescence intensity (green line, right axis). (b) De-gel time (color-coded spots) with x, y-displacements of single MagMOONs. The MagMOON plotted in (a) is marked in blue box in (b). Black stars (*) indicate the initial MagMOON position. (c) Presentation of the de-gelation process in a field view with 31 MagMOONs by plotting their x and y-positions with their de-gel time (color-coded). The de-gel time increased from the left to the right side of the figure indicating the de-gelation occurred gradually from the left to the right. The average de-gel time was 474 ± 18 s. (d) Plot of the average intensity of 31 MagMOONs (green line) and average intensity of the whole field view (blue star line). The intensities were normalized to aid comparison. The de-gel time determined by the average intensity of these 31 particles agrees with that generated from the average intensity of the whole field view.

The variation in de-gel time after adding alginate lyase is also presented in **Fig. 2.4b**. The color distribution indicates the de-gelation occurred from the top-left corner first then it went down on the left before spread out to the right. From the data in **Fig. 2.4b**, one can tell that all five particles have similar movement. This observation fits well with the previous discussion of **Fig. 2.4a** about convection current and suggests that the whole gel flowed over the cover glass before the MagMOONs became free to rotate. An advantage of using MagMOONs over un-modulated probes is that MagMOON orientation could be tracked based on their blinking signal even when the gel moves.

Although these experiments tracked the intensity change from each MagMOON, all the MagMOONs responded in a similar time frame and the rotation was synchronized to the driving field, thus the average de-gelation time can also be obtained from the ensemble average intensity. To characterize the process of de-gelation by alginate lyase, a total of 31 particles in a field of view were tracked using our particle tracking algorithm. The algorithm calculated x, y-displacements, intensity and de-gel time (defined as 20% of maximum modulation). All the experiment parameters were the same as in **Fig. 2.4a and b**. **Fig. 2.4c** shows the de-gel time distribution across the field view. The average de-gel time was 474 ± 18 s. Much of this variation appears co-ordinated, with shorter times on the left than the right of the view. **Fig. 2.4d** shows that the average de-gel time determined by the average intensity of these 31 particles also agreed with that generated from the average intensity of the whole field of view.

The above tests demonstrated a simple way to detect the de-gelation process using MagMOON modulation. The MagMOONs probed both the local and overall behavior of

the de-gel process. In additional experiments, we moved a step further by testing the detection ability through different thicknesses of chicken breast. Although the position of individual particles cannot be detected through thick tissue, the total blinking signal from many particles can.

De-gelation tracking through tissue

Unlike conventional fluorescent dyes, untethered MagMOONs emit modulated fluorescence intensity in response to a rotating external magnetic field. This blinking property distinguishes the MagMOONs signal from the tissue autofluorescence backgrounds. To determine if the blinking MagMOON signal could be detected through tissue, we placed a film of MagMOONs in a temperature-controlled chamber between two slices of chicken breast, 1 cm thick on top (to limit light escaping) and various thicknesses of 1 mm, 1.5 mm, 2.5 mm, 4 mm, and 6 mm at the bottom. During the acquisition, the temperature was maintained at 37 °C for fast and efficient enzymatic activity of alginate lyase (90). **Fig. 2.5** shows the experimental setup schematic (a) and picture (b). As mentioned in the Experimental section, we used a 514 nm laser at the power of ~ 50 mW as the excitation source and the emission signal was collected using a spectrometer. Although the background from tissue autofluorescence was high, the modulated probe spectrum can be revealed by subtracting the average signal in the dim orientation from the average signal in the bright orientation (**Fig. 2.5c**).

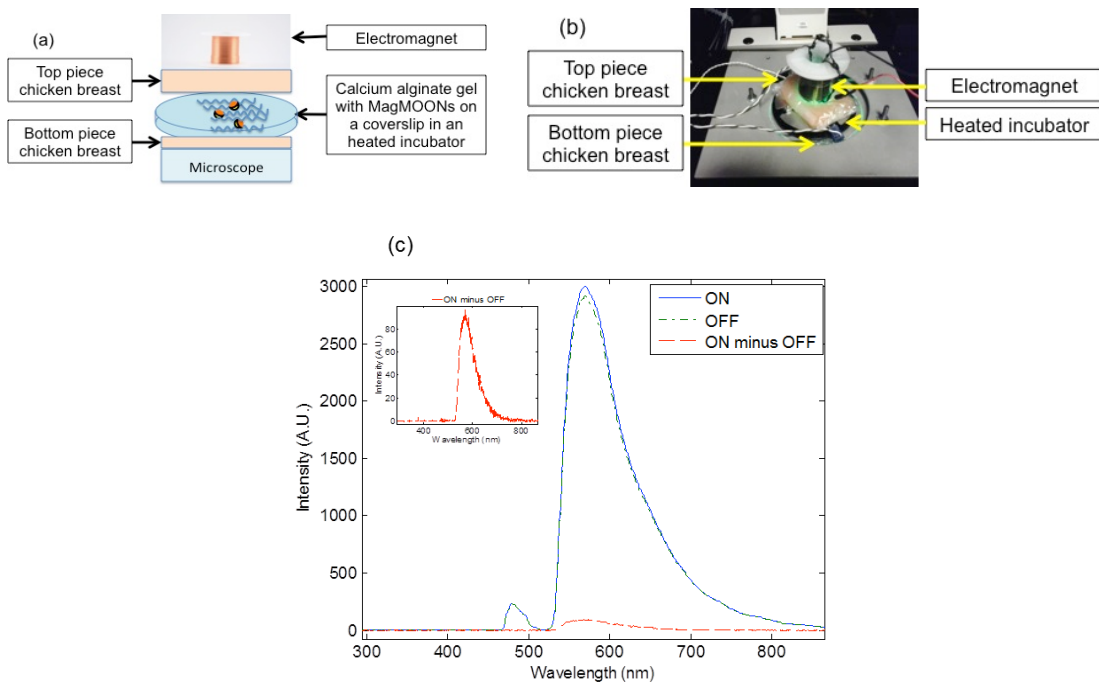


Fig. 2.5. Fluorescent imaging through turbid chicken breast tissue. (a) Schematic of the setup for magnetic modulation and imaging through tissue. The MagMOONs are trapped in alginate calcium gel on a coverslip in an on-stage incubator chamber. This chamber is embedded in the chicken breast tissue. An electromagnet was used to modulate the MagMOONs. (b) Photo of the experimental setup. (c) Representative fluorescence spectra of MagMOONs embedded beneath 1 mm tissue, acquired after de-gelation. ON and OFF is the average signal when the MagMOONs face the uncoated side and coated side, respectively, to the objective lenses. The inset figure shows the zoom-in of the ON minus OFF modulated signal.

To ensure that only active alginate lyase caused de-gelation, a control experiment was conducted using denatured lyase. Alginate lyase was denatured by boiling for 30 minutes before adding to the gel, followed by water addition to confirm that denatured lyase did not cause MagMOONs to become free to rotate. After performing these denatured lyase controls, active alginate lyase was added at 36 minutes, which caused de-gelation. **Fig. 2.6a** shows the intensity change with time of MagMOONs through 3 mm

chicken breast during four stages of the experiment. Stage 1: During the first 7 minutes of the acquisition when calcium alginate gel was covered by a 100 μm water layer, the fluorescence from the sample (tissue containing MagMOONs) bleached quickly with no evidence of modulation. Stage 2: Throughout the 20 minutes after denatured alginate lyase addition, there wasn't a significant change except for the short term restoration of background fluorescence, likely due to small shift in tissue position directly in the laser beam, followed by approximately exponential slowdown bleaching. Stage 3: The same situation occurred after denatured alginate lyase removal and water addition. Stage 4: After addition of 2 mg/mL alginate lyase, strong MagMOON modulation was observed at the driving frequency. A short-time Fourier transform was applied to the intensity-time series to clearly present the MagMOONs modulation before and after alginate lyase addition (**Fig. 2.6b**). Stage 4 clearly shows modulation at the driving frequency of 0.25 Hz, as well as higher frequency harmonics arising from driving the modulation with a square-wave modulated magnetic field. For clarity, **Fig. 2.6c** shows the intensity of 3 represented frequencies, of which one is corresponded to the modulated frequency and two nearby frequencies (0.22 and 0.45 Hz). The strength of the 0.25 Hz frequency component is clearly higher than the background at 0.22 and 0.45 Hz.

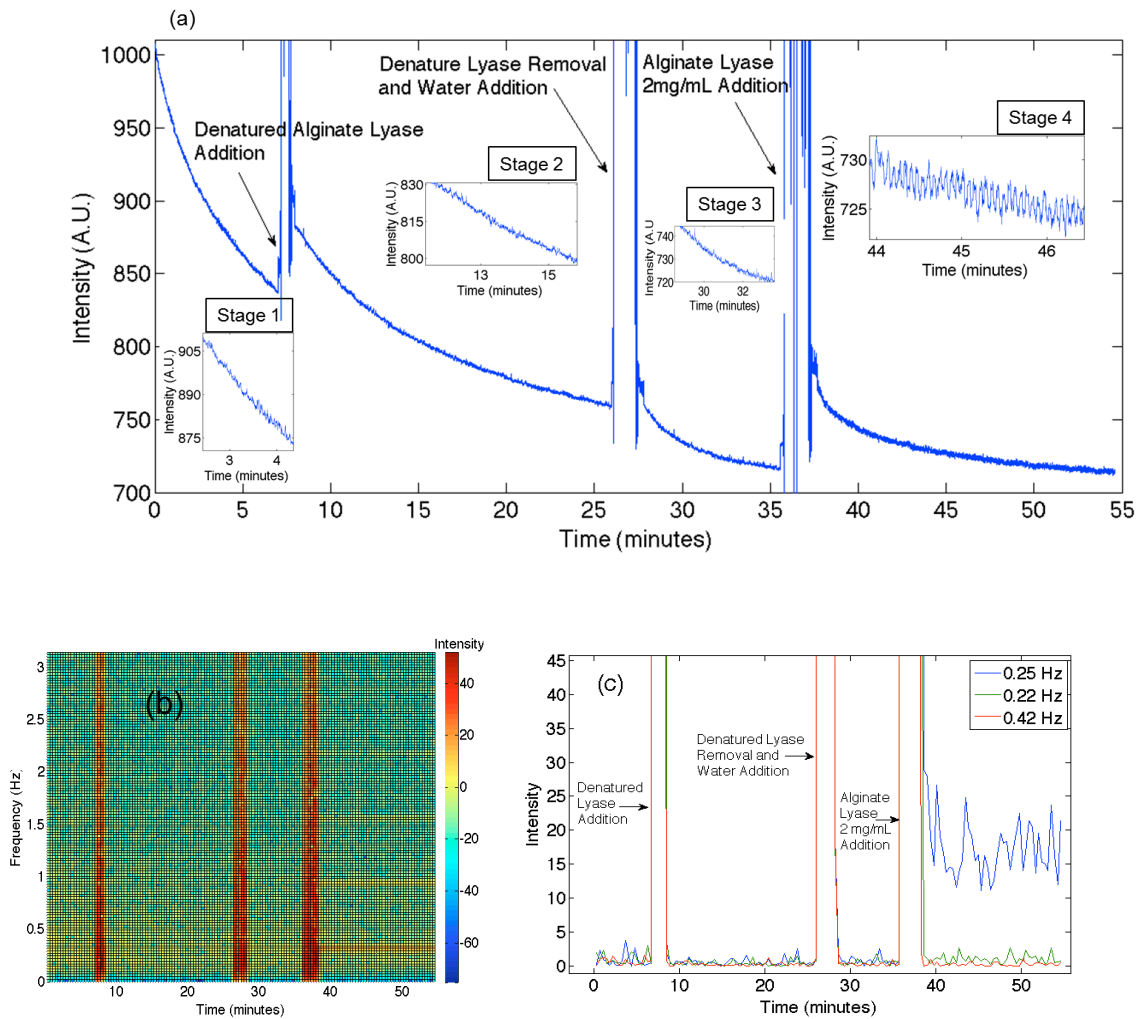


Fig. 2.6. Monitoring of MagMOON modulation through tissue after adding denatured and active alginate lyase to the alginate gel. a) Magnetically modulated fluorescence signal through 3 mm of chicken breast using 514 nm green excitation laser during 4 stages: Stage 1: alginate gel in water; Stage 2: after adding denatured alginate lyase; Stage 3: after denatured alginate lyase removal and water addition; Stage 4: after 2 mg/mL alginate lyase addition. Modulation can be seen during Stage 4. Inset figures are zoom-ins to show modulation if present. b, c) Short-time Fourier transform spectrogram shows modulation after alginate lyase addition but not after addition of water or denatured alginate lyase.

Having successfully detected alginate lyase activity through 3 mm of chicken breast, we next studied how tissue thickness affected signal intensity. The setup was the same as shown in **Fig. 2.5** and the results are presented in **Fig. 2.7**. In **Fig. 2.7a**, the fluorescent signal through 2.5 mm tissue is plotted with a smoothed curve of the original data. After subtracting with the smoothed curve to take into account for the bleaching background, the modulated and background-corrected signals through 1 mm, 1.5 mm, 2.5 mm, 4 mm and 6 mm are presented in **Fig. 2.7b,c**. Although the amplitude of modulation decreases dramatically with the increase of the tissue thickness, the modulation is clear through up to 4 mm (see the inset figure of **Fig. 2.7c**). We used short-time Fourier transform to elucidate the de-gel points (**Fig. 2.8**) and obtained the values of about 5, 10, 11 and 7 minutes following lyase addition through 1 mm, 1.5 mm, 2.5 mm and 4 mm tissue, respectively. This time range agrees with the SPT results, where modulation can be seen after 5 - 12 minutes (data not shown). Most of this variation is likely due to subtle differences in gel preparation. As prepared, the gel system is able to detect alginate lyase at 2 mg/mL or 60.6 μ M concentration (given the molecular weight of alginate lyase is 33 kDa (90)) in 10 minutes. **Fig. 2.7d** shows the signal to baseline noise ratio as a function of tissue depth, where the signal is defined as the difference between the 0.25 Hz Fourier series coefficient after de-gelation and at the start of the experiment (while the MagMOONs were still entrapped), and the baseline noise is defined as the standard deviation of the 0.25 Hz Fourier series coefficient at the start of the experiment. The signal-to-baseline-noise ratio decreases by approximately one order of magnitude per millimeter of tissue depth; we expect it can be improved by acquiring signal over longer

periods of time (e.g. using a longer window in the short-time Fourier transform), using red-excited fluorophores, increasing the optical collection efficiency with a large area photodetector in place of the narrow-slit spectrometer, increasing the number of MagMOONs, or mechanically compressing the tissue). Nonetheless, the study confirmed that the MagMOON signal could be tracked through tissue to detect the presence of alginate lyase.

Fig. 2.8 shows the 3-D plots of relative Fourier component amplitude (log scale, color-coded) as a function of frequency time for all studied tissue thickness (a) and corresponding plots of relative Fourier component amplitude in time at the driving frequency (0.25 Hz) and two non-modulating frequencies (b). Modulation can be seen after 5, 10, 11 and 7 minutes with 1 mm, 1.5 mm, 2.5 mm and 4 mm tissue respectively.

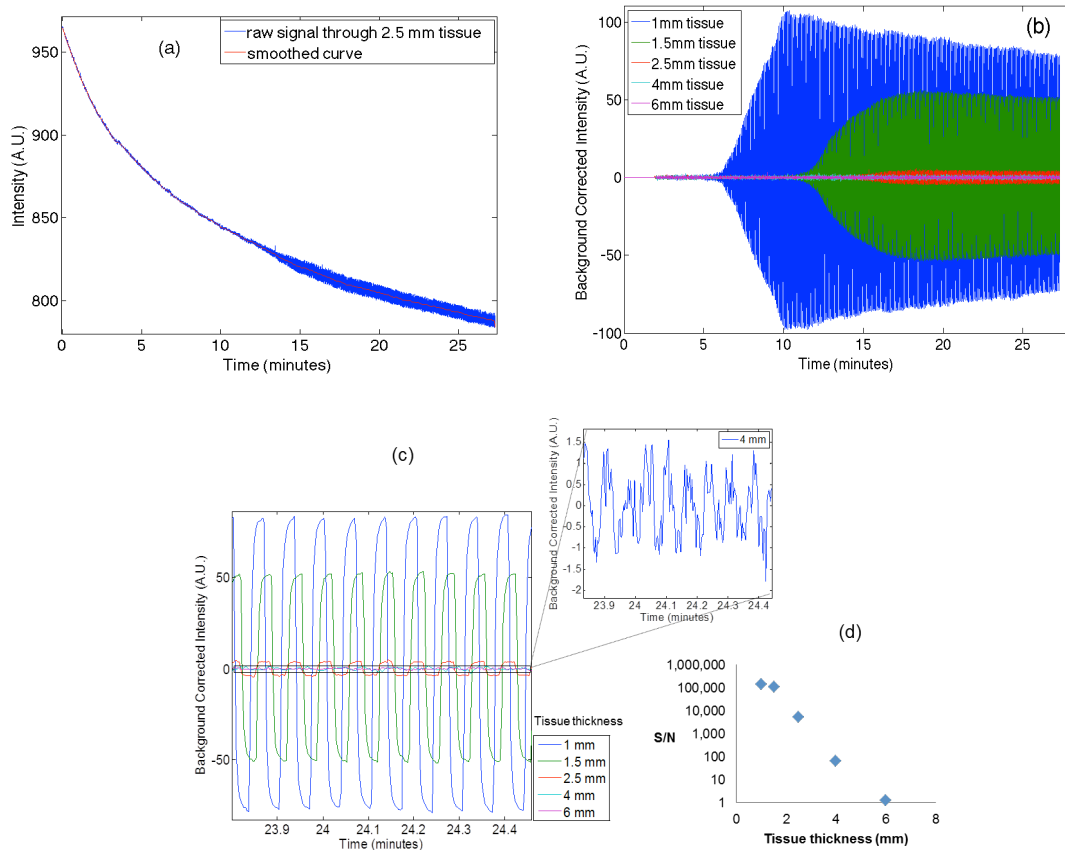


Fig. 2.7. Detection through tissue the de-gelation by alginate lyase. (a) Plot of fluorescence signal through 2.5 mm chicken breast and its smoothed curve. (b) Background-corrected magnetically modulated fluorescence signal through 1 mm, 1.5 mm, 2.5 mm, 4 mm and 6 mm chicken breast. (c) Zoom-in of (b) to visualize modulation. The inset figure is a more zoomed-in of the 4 mm tissue thickness case for clarity. (d) Signal to baseline noise ratio for MagMOONs viewed through different tissue thicknesses, based upon Fourier analysis in Fig. 2.8.

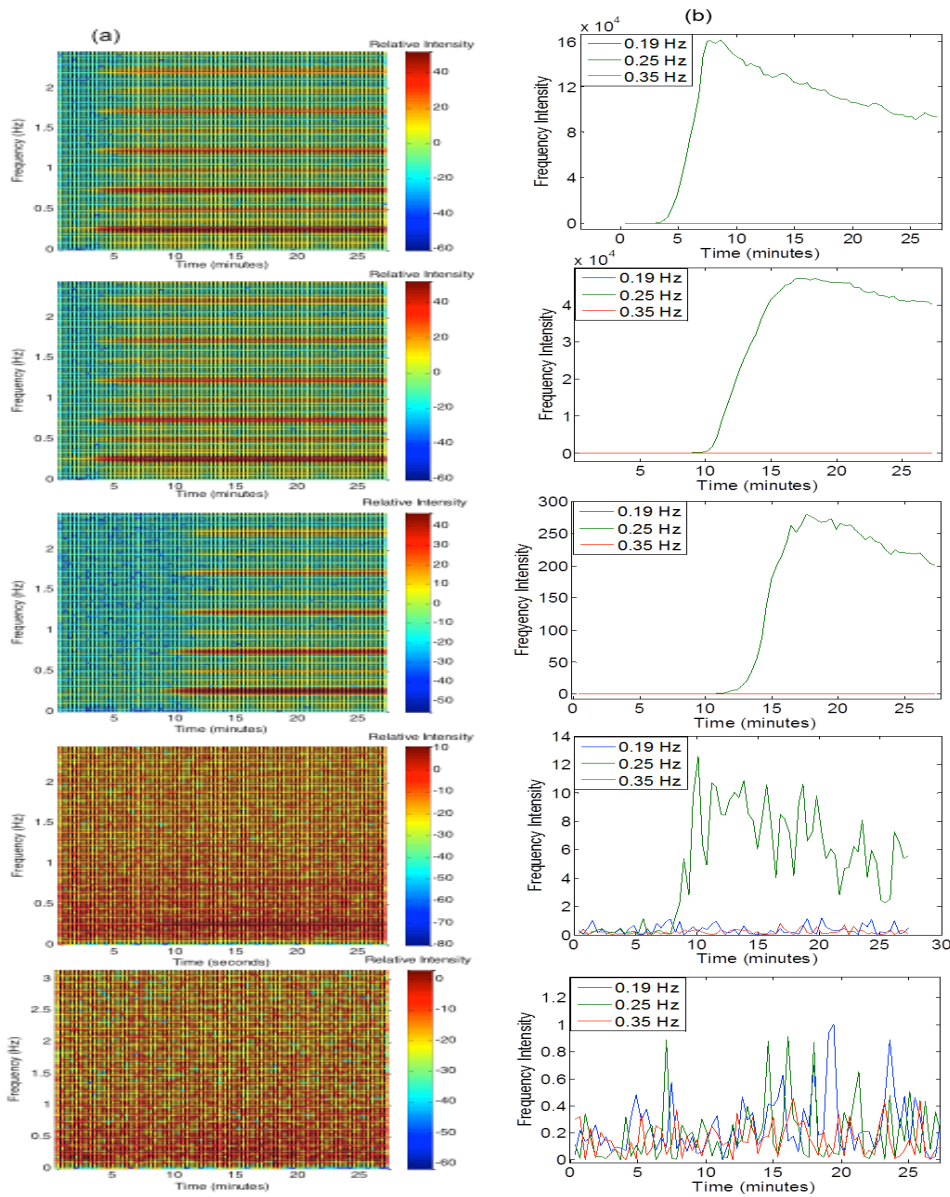


Fig. 2.8. Short-time Fourier transform analysis to detect blinking through tissue. Short-time Fourier transform spectrogram (73 windows, each 23 s long) of fluorescent intensity through 1 mm, 1.5 mm, 2.5 mm, 4 mm and 6 mm tissue (from top to bottom) following alginate lyase addition. Modulation is evident through up to 4 mm tissue. (a) 3-D plot of relative Fourier component amplitude (log scale, color-coded) as a function of frequency time. (b) Plot of relative Fourier component amplitude in time at the driving frequency (0.25 Hz) and two non-modulating frequencies. Modulation can be seen after 5, 10, 11 and 7 minutes with 1 mm, 1.5 mm, 2.5 mm and 4 mm tissue respectively.

Conclusions and Future Work

We developed a simple yet novel means to detect alginate lyase activity based upon the change in MagMOONs modulation in alginate gel before and after alginate lyase addition. The blinking MagMOON signals can be observed through tissue and separated from autofluorescence. Although we only detected through 4 mm of tissue, we used a microscope-coupled spectrometer with very small optical collection efficiency due to the small field of view and numerical aperture. In future, we plan to use large-area photomultiplier tubes with a lock-in amplifier for more sensitive measurements in thicker tissue. For single particle studies *in situ*, an endoscope will be used to collect fluorescent signals from MagMOONs through tissue. This approach could also be expanded to red-excited fluorescence, X-ray excited optical luminescence (91), and SERS (92).

CHAPTER THREE
TRACKING ANISOTROPIC OPTICAL TRACERS (MOONS) TO STUDY
INTRACELLULAR TRANSPORT AND CYTOTOXICITY

Introduction

This section will start with a short introduction of macrophages, cytoskeletal structure and protein motors. The roles of intracellular transport and related diseases are then presented, following with a brief review of intracellular transport study. Finally, the cytotoxicity of three cytoskeletal drugs used in this study: cyanide, azide and 2-deoxy-D-glucose will be summarized.

Macrophages

Macrophages are phagocytic cells that keep the body clear of intruding foreign matter. They originate from hematopoietic stem cells in the bone marrow. Lung macrophages include pleural, intravascular, interstitial and surface (airway and alveolar) macrophages. Among them, the surface macrophages are exposed to the environment the most and hence are the first barriers of the defense system, with the function of engulfing, transport and clearance of particulate matter entering via the respiratory tract (93). The mechanisms of these particles to enter cells (endocytosis processes) can occur through pinocytosis, micropinocytosis and phagocytosis; particles larger than 250 nm in diameter are generally taken up by phagocytosis. Phagocytosis can be non-specific or receptor-mediated (e.g., mediated via binding of cell receptors to complement molecules adsorbed

onto the particle surface or Fc regions of antibodies bound to the surface) (94). Phagocytosis and mucociliary transport are the two main processes for lung clearance of particulate matters (95). Swanson reviewed the steps for phagocytosis: first, a particle binds to the cell membrane by either mediated receptors or electrostatic forces. Then the transfer signal is activated, following by actin functioning. Finally, a closed vesicle is formed over the particle (96). The uptake is often completed within a day (97). Once the particle is bound to the receptor, intracellular signaling activates actin polymerization and coordinates cytoskeletal movements (98). From here, the intercellular transport of the phagosome (vesicle of the particle) is carried on by protein motors along microtubules. The phagosome then is fused with lysosome where the particle is digested with lysosomal hydrolyses (94). Among these steps, intracellular transport requires the involvement of cytoskeletal structures and protein motors.

Cytoskeletal structures and protein motors

Microtubules, microfilaments (or actin filaments) and intermediate filaments are the main components of the cytoskeletal structure. Their important roles include cell structural support, movement and transport. The structures of these cytoskeletal filaments are well summarized by Alberts and others (99). Briefly, microtubules are long hollow cylinders of about 25 nm in diameter, composed from α - and β -tubulin proteins and arranged from the nucleus toward the cell membrane. Microfilaments are two-stranded helical polymers of actin protein with diameter of about 7 nm, distributed in abundance beneath the plasma membrane throughout the cell. Intermediate filaments are about 10 nm in diameter and made of different types of proteins. They help resist mechanical

stress, like the springs of a mattress. These cytoskeletal filaments are like the roads of a city although only intermediate filaments are more stable structures, whereas microtubules and actin filaments are dynamic and can be re-structured quickly. Intracellular transport on these roads is carried out by dozens of motor proteins including myosins, kinesins, and dyneins. Myosins are actin-based motor proteins that move along actin filaments. Among them, myosin II is well-known and the first identified to generate force for muscle contraction (100), while myosin V plays roles in organelle and vesicle transport (101). Dyneins and kinesins are two types of motor proteins that transport organelles along microtubules (102). Most kinesins have binding sites for membrane-enclosed organelles or for other microtubules (103). Cytoplasmic dyneins are responsible for vesicle trafficking (104) and axonemal dyneins can move the microtubules at a very fast speed (105).

Roles of Intracellular Transport and Related Diseases

As mentioned in the macrophages section, intracellular transport is essential to ensuring the regular functions of the cellular machinery by trafficking and delivery of proteins and molecules to their functional locations in cells (94). Disruption of this transport may lead to many diseases as described in (106, 107). Some examples are cystic fibrosis lung disease in which, due to mutations of the cystic fibrosis, transmembrane regulator (CFTR) gene is not transported to the right cellular location (108); and a number of neurodegenerative diseases associated with axonal transport damage such as Alzheimer's disease, Parkinson's disease, and amyotrophic lateral sclerosis (ALS) (109, 110). There are also illnesses related to viral trafficking (hijacking), where viruses such

as HIV use intracellular transport networks to invade nucleus (111, 112), or to survive and replicate while avoiding immune system responses, such as *Salmonella enterica* (113). Studying intracellular transport, therefore, is important to elucidate the mechanisms of these diseases and possibly guide therapeutic solutions.

Study of intracellular transport

Beside the need to know what cell compartments participate in intracellular transport, it is even more important to know how they function. Often, the structures involved in transport are not visible under light microscopy because their sizes are below the resolution limit. For instance, vesicle size is around 30-200 nm, and microtubule size is about 25 nm. Hence, the understandings of intracellular transport have tightly bound with the development of the microscopy and staining techniques. (114-116). In 1665 Hooke described in details many small objects in the micrometer size range that are invisible to the naked eye, including cells from a cork, using a microscope (117). Cell morphology was widely explored in the nineteenth century (115) but cell physiology describing the intracellular dynamic interactions, including intracellular transport studies, only bloomed in the twentieth century with the development of live-cell imaging techniques such as phase-contrast microscopy (118), polarization microscopy (119), and video-enhanced differential-interference contrast microscopy (120, 121). Inoué described the change of mitotic spindle and chromosome movement by microtubules during mitosis using polarized microscopy in 1953 (119). With video-enhanced differential-interference contrast microscopy (VE-DIC) the marine protist *Allogromia* dynamic microtubule movement and the fast transport along microtubules in squid axon was observed by Allen

and colleagues in 1981 and 1982, respectively (120, 121). Salmon (122) reviewed the important role of VE-DIC in the discovery of cytoplasmic protein motor kinesin in 1995.

Exploration of the microscopy techniques, especially particle tracking, has enhanced greatly the understandings of intracellular transport mechanisms. The trajectory of a tagged tracer on a vesicle, an organelle, a protein motor, or a skeletal structure is followed, and parameters such as moving velocity, MSD and correlation coefficient are widely used to characterize intracellular transport motion. Since the late 1900s researchers started to describe in more detail the intracellular transport process. Axons were the popular choice for intracellular transport study due to their fast transport (1-5 $\mu\text{m/s}$) of organelles and molecules over long distances (123). An *in vitro* test on isolated axonal filaments showed organelles of different sizes moved continuously along the filaments with the same velocity of $\sim 2 \mu\text{m/s}$. Meanwhile, in intact axoplasm organelles moved discontinuously and the speed was size-dependent, with the larger organelles (such as mitochondria) moving at a slower rate than smaller vesicular organelles (124). These results implied the existence of a highly interconnected filament system in cytoplasm that hinders large organelles more than smaller ones. In a review in 1987, Vale listed the velocity of movement ($\mu\text{m/s}$) of different motility proteins as: skeletal muscle myosin (2-5); *Acanthamoeba* myosin I (0.03); ciliary dynein (10); cytoplasmic dynein (1) and kinesin (0.5). Here we can see that the moving velocity can be up to 3-fold different, depending on the type of motor.

Allan and colleagues (125) described in detail quantitative results on early endosome transport by SPT. They divided the tracers' motions into two groups, run and

rest by the thresholds of moving rate of 0.17 $\mu\text{m/s}$ and moving length of 85 nm. Motions with higher numbers than these thresholds are defined as runs while lower ones are rests. By these definitions, they claimed, on average, endosomes in HeLaM cells run for 22% of total time; with 65% of a total of 1800 labeled endosomes having at least 1 run during data collection. Treatment with nocodazole to depolymerize microtubules caused no observed linear movement, suggesting all runs were along microtubules. They also reported the fastest observed speed was 8 $\mu\text{m/s}$ while the corresponding estimated value in mammalian cells was $\sim 4\text{-}5$ $\mu\text{m/s}$ according to (126). With the same objectives when tracking early endosome trafficking on human epithelial cells, Holzbaur and others (127) had a different motion classification. First, they classified the motions into three categories: directed, diffusive and confined, instead of two. Directed motion moved faster than 1 $\mu\text{m/s}$ and the confined motion moved less than 0.5 μm . The classification was based on the scaling exponent α value, obtained from fitting the MSD with Equation 2.

$$\text{MSD} = \langle r^2 \rangle = 4Dt^\alpha + 2\sigma^2, \text{ (Equation 2)}$$

where D is the diffusion coefficient, t is the time lag, and σ is the measurement error. Motion with $\alpha > 1.45$ is directed, $\alpha < 0.4$ is confined, and in the middle range is diffusive. They found that 59% of motions are confined; 39% are diffusive (at pauses) and only 2% are directed. They also found that during the transition time before and after a directed run, the motion is diffusive. In 2012, the Fang group published their study on axonal transport with nanorod rotational tracking. They found that the nanorod orientation was maintained during the active transport. They also observed long pauses and short pauses of the transport where the long pauses were associated with rotation. Moreover, 76% of

long pauses with rotation were followed with a direction reversal. This indicated there might be uncoupling and reattachment of motors during long pauses in preparation for the change in direction (128). These findings emphasized the extended information provided by the rotational tracking in compliment with translational tracking. Therefore, we expect our rotational and translational tracking method will reveal useful information about intracellular transport that can be used to evaluate cytotoxicity. To test this hypothesis, we will use cytoskeletal drugs – 2-deoxy-D-glucose with either cyanide or azide to inhibit intracellular motion. The toxicity mechanism of these compounds is described in the following section.

NaCN, NaN₃ and 2-deoxy-D-glucose toxicity

As tracers are phagocytized, phagosomes containing these tracers are formed and transported within cells by molecular motors that move along cytoskeletal structures (e.g., myosin V moves along actin filaments). This motion can be inhibited by depletion of ATP production. NaCN or NaN₃ are toxins that reduce ATP production by inhibiting electron transport when binding to the cell's cytochrome oxidase complexes (129). Meanwhile 2-deoxy-D-glucose, with a similar structure to glucose competitively inhibits glycolysis and therefore stops the free energy generation required for ATP synthesis (130). The combination of these two inhibitors was reported to cause a huge depletion of ATP production compared to separate use (131-133). This energy depletion in turn has a significant effect on macrophage transport. We use both inhibitors as a positive control for the cytotoxicity assays.

Method and Experimental Setup

MOONs preparation

The 520 nm fluorescent Dragon Green particles were purchased from Bangs Laboratories (Bangs Laboratories, #SF03F, Inc., Fishers, IN). The particles comprised Dragon Green fluorescent dye (480, 520) entrapped in polystyrene beads. Modification of these particles into MOONs is similar to that described in Chapter Two. Briefly, 10 μL of 520 nm fluorescent particles 1% w/v dispersion in water was mixed with 240 μL ethanol using a vortex mixer, deposited evenly onto six 25 mm-coverslips, and allowed to dry. A layer of aluminum was deposited onto the coverslips using an Auto 306 (BOC Edward, West Sussex UK) thermal vapor deposition system. During this process, aluminum vapor from a heated tungsten boat travels ballistically through vacuum to coat the glass coverslips as well as the top hemisphere of the fluorescent particles on the coverslip. The thickness of the aluminum layer was measured during deposition using a 6 MHz quartz crystal microbalance; deposition was stopped at 30 nm. After deposition, 20 μL water was pipetted on the coverslip with freshly prepared MOONs. The area in the drop was brushed with a camel hair #0 paintbrush to gently removed particles from the coverslip surface. The suspension was then carefully transfer into a 1.5 mL centrifuge tube by pipetting and DI water was added with the ratio of 70 μL per coverslip, followed by sonication of the paintbrush immersed in the suspension. MOONs from this suspension were added to the cell medium.

Chemicals

Sodium cyanide (NaCN), reagent grade, 97% and 2-deoxy-D-glucose were purchased from Sigma Aldrich (St. Louis, MO). Sodium azide (NaN₃) 5% w/v solution was from BDH (West Chester, PA). For the cytotoxicity experiments, 7.5, 15, 30 or 45 μL CuO 5mM; 62.5 μL NaN₃ 0.1 M and 62.5 μL 2-deoxy-D-glucose 0.1 M; or 142.8 μL NaCN 0.05 M and 71.4 μL 2- deoxy-D-glucose 0.1 M were added to 500 μL media before imaging.

Cell culture

J774A.1 macrophages were purchased from American Type Culture Collections (ATCC, Manassas, VA). The cells were cultured for 48 hours before imaging in Dulbecco's modification of Eagle's medium, 1X with 4.5 g/L glucose, L-glutamine, & sodium pyruvate (Mediatech, Inc., Manassas, VA) supplemented with 10% heat inactivated fetal bovine serum (Thermo Scientific, Logan, UT), penicillin (100 units/mL) and streptomycin (100 μg/mL). The cells were grown on a 8 well Lab-Tek chamber slide (#177402, Electron Microscopy Sciences, Hatfield, PA) and maintained at 37 °C, 5% CO₂. MOONs were added in cell wells one day before imaging to ensure most of them were phagocytized by macrophages by the imaging time (97, 134-136). The MOONs outside cells were washed away when changing to the new completed DMEM cell medium before acquisition. For the cytotoxicity experiment, the completed DMEM cell medium was replaced by Dulbecco's modification of Eagle's medium, 1X without glucose, L-glutamine, & sodium pyruvate (Mediatech, Inc., Manassas, VA).

Live-cell imaging

The microscope setup is the same as described in **Fig. 2.1f**. A Nikon Eclipse Ti-E microscope (Nikon Instrument Inc., Melville, NY) with a 10 ×, 0.45 NA objective lens was used for all experiments. Imaging acquisition was set at binning 1, display (1392 × 1040 pixels). While imaging MOONs in cells on the microscope stage, cells were maintained at 37 °C, 5% CO₂ in a chamber of a Live Cell stage top incubator (Pathology Devices, Inc., Westminster, MD). The sample was illuminated using blue light excitation from a filtered mercury lamp and images were continuously acquired every 0.2 sec (0.2 sec exposure time) using a CoolSnap HQ2 high sensitivity quantitative monochrome camera and the Nikon imaging software NIS-Elements (Nikon Instrument Inc., Melville, NY). Acquired time-lapse images were exported in multi-TIF format and a custom Matlab scripts were written to extract from the acquired fluorescence movies the position and fluorescence intensity of single particles in time.

The particle position was determined from the intensity centroid within a region around the particle, after applying a threshold to remove background signals. The total intensity of the tracked region was also recorded. Although all particles in view could be tracked simultaneously, to ensure comparable data, we selected for tracking only particles that were well separated (more than 2 particle diameters), and stayed in the field view and within a certain range of focus. In addition, we removed a few rare particles that didn't blink (either because they were uncoated or stuck to the glass), or had paths that crossed each other. Using these selection criteria, on average ~ 40% of the particles in view were track-able.

Analysis of Data from Particle Tracking

From thousands of time lapse images we used a custom particle tracking script to extract x,y-coordinates (trajectory) and intensity of each individual particle at each time point, and stored them in multi-dimensional arrays as Mx, My and meanI respectively. These outputs are then be used to calculate various parameters that are meaningful in characterizing the particle motion. The parameters include mean squared displacement (MSD), diffusion coefficient (D), velocity (v), and histogram.

Results and Discussion

Rotational and translational tracking of single tracers reveals intracellular transport mechanisms

The 520 nm Dragon Green fluorescent particles were fabricated into MOON tracers for rotational and translational tracking. They were added to cell wells 24 hours before imaging to ensure all MOONs were phagocytosed. Macrophages containing MOONs were maintained at 37 °C and 5% CO₂ during fluorescent imaging for about 5 min with a rate of 5 frames per second. Outputs extracted from the image series include x, y-coordinates and the average intensity surrounding each MOON at each time point. Tracking is difficult if the particles' trajectories cross. Therefore, the particles' concentration adding to cells was limited so that each cell had about one or two particles. **Fig. 3.1** shows a superimposed image of cells and MOONs where there are not too many

MOONs in a cell. In addition, by the time of acquisition, there were no particles outside cells.

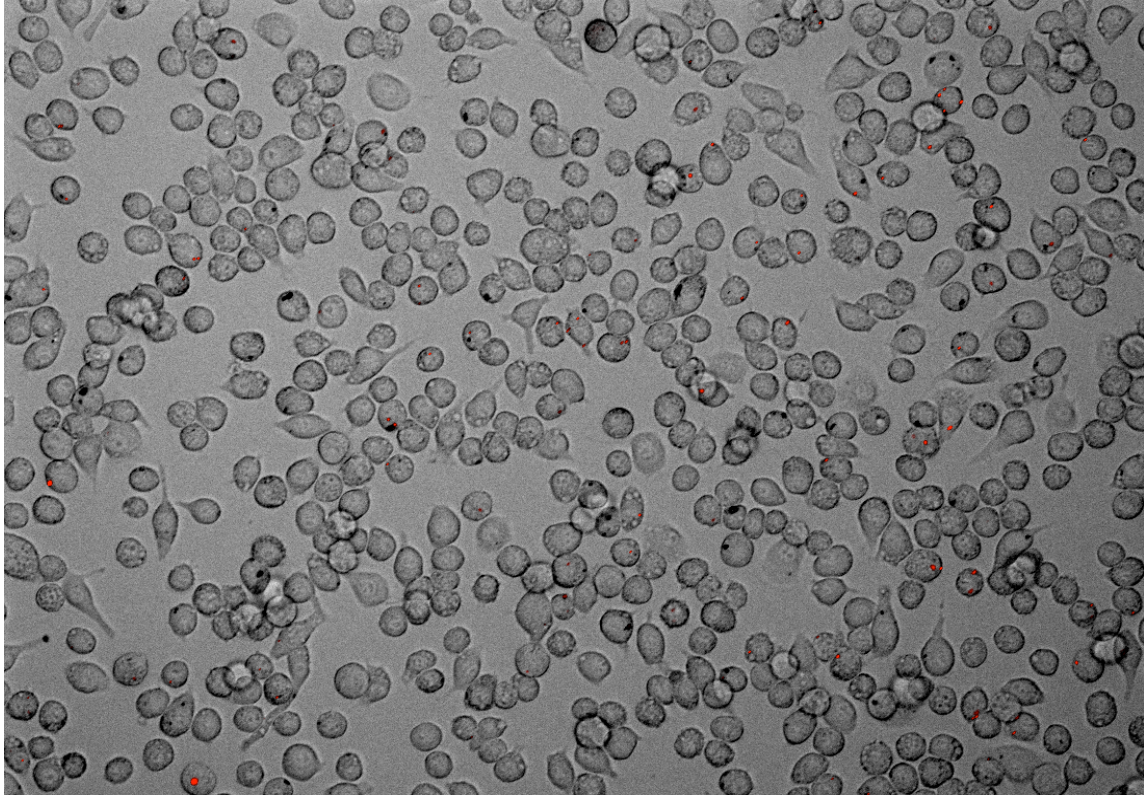


Fig. 3.1. Superimposed image of macrophages in transmitted light bright field (gray) and fluorescence from MOONs (red).

Fig. 3.2 shows the relationship between rotation and translation of an individual MOON via x, y-coordinates and mean intensity plots. There are 3 types of behaviors presenting in the MOON's motions. Type (I) motion has fast and straight position changing but the change in intensity is not significant, indicating non-rotation when sliding behavior. This should be the case when the MOON was sliding along a microtubule. Type (II) motion, on the other hand, has clear changes in intensity but the position doesn't change significantly, indicating the rotate-not move behavior. This

observation is in agreement with the pause periods in Fang's group study on axonal transport (128), suggesting a motor switching mode. Notably, after the second rotation highlighted in the second block of type (II) in **Fig. 3.2**, the x and y-coordinates started changing, implying the pause was for tethering the MOON onto a (new) motor. There is also type (III) when both position and intensity are not changing which could simply be the case when the particle is resting and not linked to a motor, or the tracking is lost. This result on tracking a single MOON shows that our approach can obtain similar behaviors previously reported. Moreover, tracking the rotation and measuring the rotation rate of a single MOON in a macrophage was also used to investigate the cytotoxicity of cyanide (Appendix A).

Observation over an ensemble of MOON tracers shows the global characteristics of that population and can be used to distinguish different populations

The previous section presents single-MOON behavior in a cell. We can characterize the whole population as well. As an example, we compared the MOONs motion in cells and in glycerol. Since the motion in glycerol is random, we also simulate Brownian motion and compare the three results together.

MOONs were dispersed in ~ 80% glycerol and a capillary was filled with MOONs in glycerol by dipping in the suspension. This capillary was sealed at its two ends to ensure the system is closed and reaches equilibrium before imaging with the same conditions as the in cell experiments. For simulated particles, x, y-coordinates were generated by using random function in Matlab (randn), and the random intensity was generated by function $I = [1 + \sin(\theta)] \exp[-(x^2 + y^2)/s^2]$, where θ is the rotation angle, x, y

are the displacements and s is the standard deviation. The diffusion coefficient of these simulated motions is $0.151 \text{ } (\mu\text{m}^2/\text{s})$.

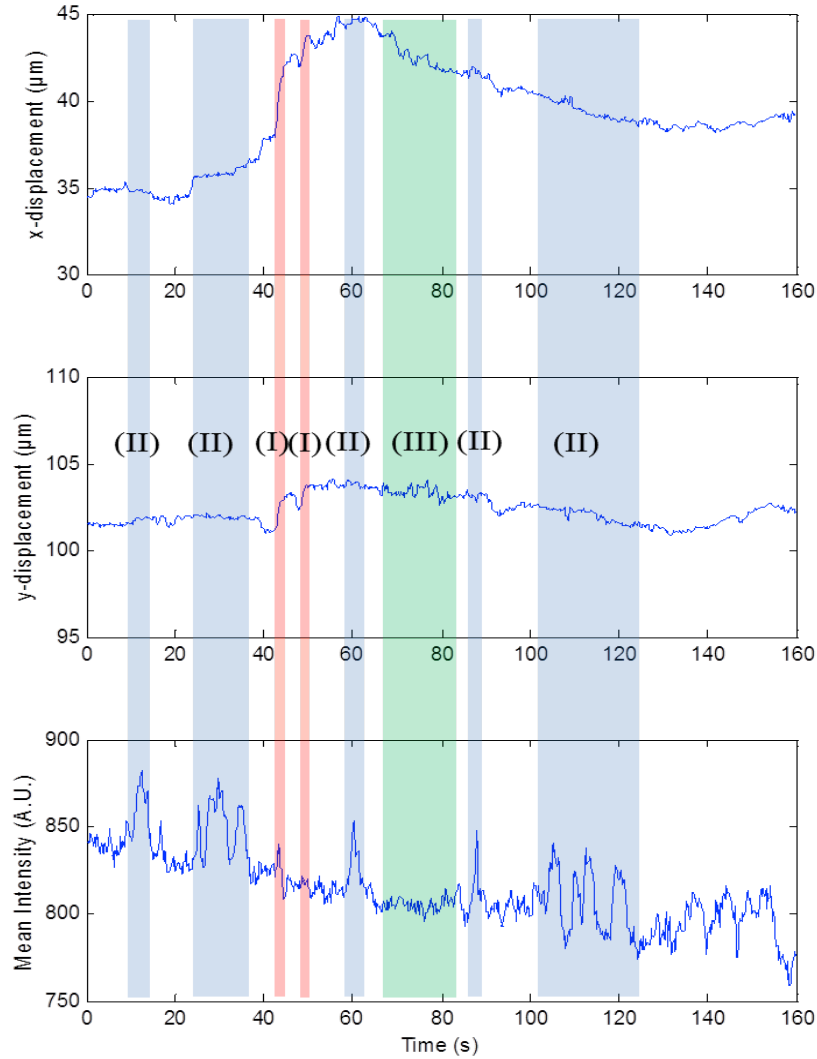


Fig. 3.2. Position and intensity change of a single MOON particle with time.

From the x, y-coordinates and intensity, we calculated the translational (along the x-axis, for instance) and rotational (intensity) velocity after every 10 frames (2 s) of eight

randomly picked MOONs from each data set for comparison of their correlation (**Fig. 3.3**).

The shape of the scattering plot between intensity change and velocity in cell is diamond-like (**Fig. 3.3a**) whereas those of in glycerol and random simulation are oval (**Fig. 3.3b and c**). The oval shape agrees with random motion. With the diamond-like shape, there are more data points distributed parallel with x and y-axis and symmetric around the zero points, implying more cases of either type (I) or type (II) motion, where the motion in cells is more directed than diffusive. In addition, the amplitude of velocity and intensity change of MOONs in cell is significantly smaller than that in glycerol. Hence, the correlation between translational velocity and rotational intensity change can be an index to characterize a large population.

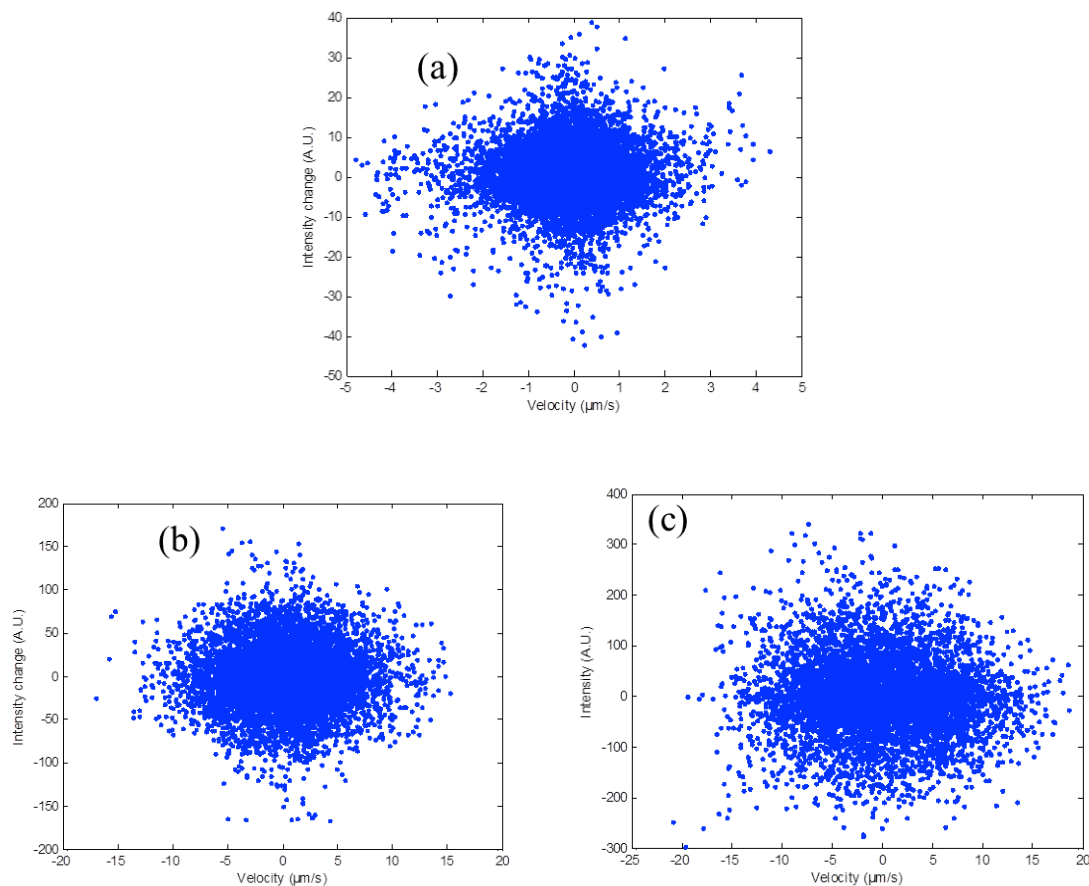


Fig. 3.3 Correlation between velocity and intensity change of MOONs in cells (a), in glycerol (b), and by simulation (c).

Cytotoxicity of 2-deoxy-D-glucose in combination with either cyanide or azide

To validate our method of studying cytotoxicity using rotational and translational SPT, we used ATP inhibitors to stop the intracellular transport. Before the imaging acquisition, either NaN_3 10 mM and 2-deoxy-D-glucose (10 mM); or NaCN (10 mM) and 2-deoxy-D-glucose (10 mM) were added to 500 μL medium. Both sets of drugs caused immediate immotile behavior of cells and therefore particles. For simplicity, only the result with (NaN_3 and 2-deoxy-D-glucose) case will be presented and regularly called “toxin” in this manuscript.

There were 36 MOONs tracked in the toxin addition case. Their trajectories are plotted in **Fig. 3.4a**. These trajectories appear as small dots and the MOONs' movement is hardly detected because the toxins inhibited the particles' motion. For visual comparison, trajectories of 58 tracked MOONs in cells with no toxin addition as a control were also plotted (**Fig. 3.4b**). Although the motion in the control varies among particles, it is clear that the MOONs' moving amplitude is larger compared to when toxins are added. In the next section the quantitative analysis based on mean squared displacement (MSD) to classify the different types of motion in each sample will be presented.

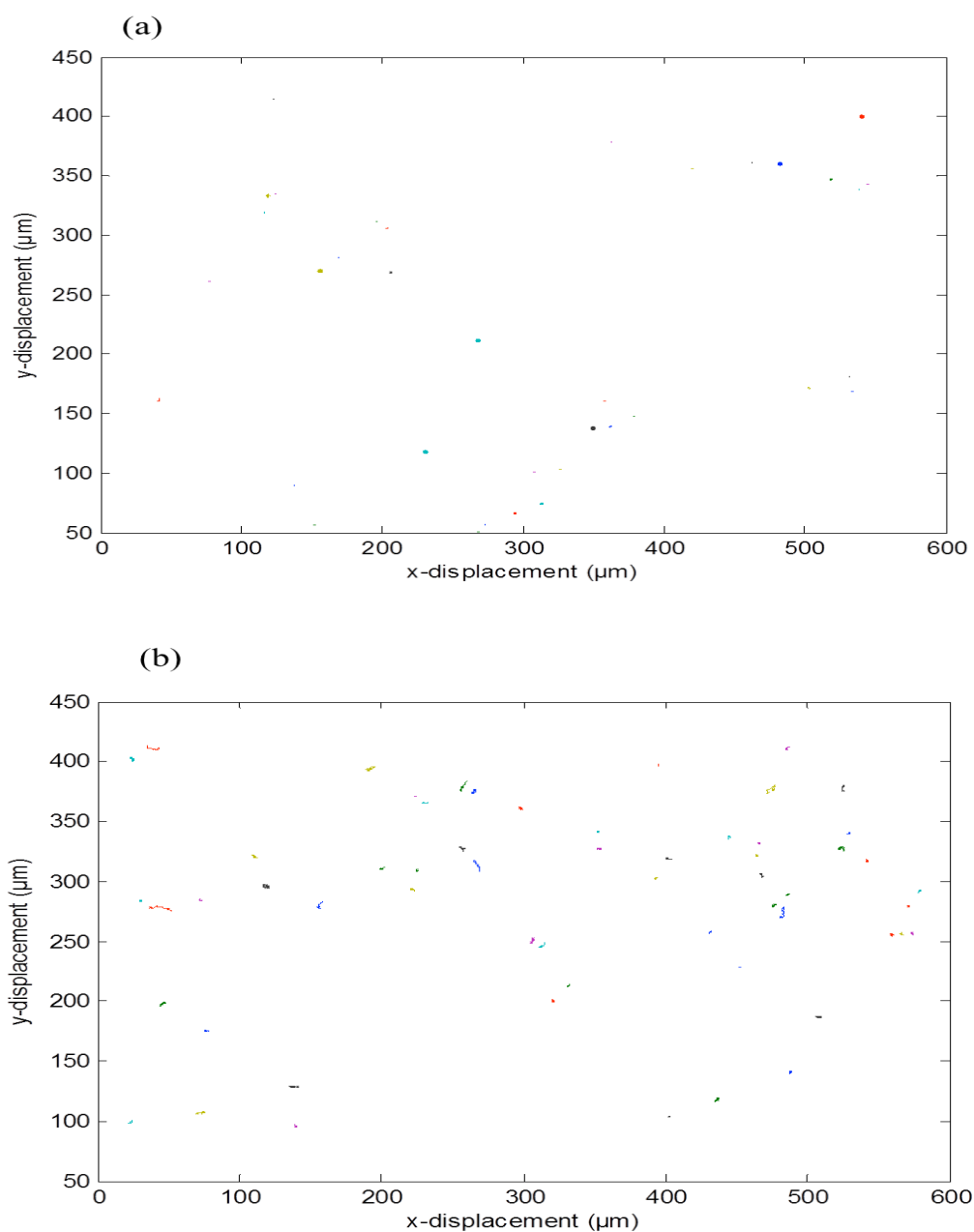


Fig. 3.4. Trajectories of MOONs in macrophages with $(\text{NaN}_3 + 2\text{-deoxy-D-glucose})$ addition **(a)** and no toxin addition **(b)**.

Motion classification and quantitative characterization of motion

To quantitatively analyze the motion the MSD was calculated for each sub-trajectory extracted from a whole length trajectory of each particle (Matlab script in

Appendix D) and fit them using a non-linear least-squares data-fitting function in MATLAB named `lsqcurvefit`. Based on the results of this fitting, important parameters such as velocity or the scaling exponent (α) were used to classify different motion types of each sub-trajectory (Matlab script in Appendix E). The percentage of each type of motion over all sub-trajectories of a population can be a good indicator to characterize that population's properties.

MSD is the average of the squared distances a particle moves over time along its trajectory. Its formula is given by $MSD = \langle r^2 \rangle = \langle (r_1 - r_2)^2 \rangle$, where r_1 , r_2 are the particle's position after a time lag t (s) and the $\langle \rangle$ sign indicates an average. MSD is a very useful tool to characterize particle motions.

The four typical models for motion are directed motion, normal diffusion, anomalous diffusion, and confined diffusion and each is described by the equations below, as reviewed in (43).

Directed motion: $MSD = \langle r^2 \rangle = 4Dt + v^2t^2$ (Equation 3)

Normal and anomalous diffusions: $MSD = \langle r^2 \rangle = 4Dt^\alpha$, (Equation 4)

where α is the scaling exponent, $\alpha = 1$ for normal diffusion and $\alpha < 1$ for anomalous diffusion.

Confined diffusion: $MSD = \langle r^2 \rangle = [1 - A_1 \exp(-4A_2Dt/\langle r_c^2 \rangle)]$, (Equation 5)

where $\langle r_c^2 \rangle$ is an estimation of the confinement size, and A_1 , A_2 are two constants determined by the confinement geometry. In all equations, D is the diffusion coefficient ($\mu\text{m}^2/\text{s}$), t is the time lag (s), and v is the velocity ($\mu\text{m}/\text{s}$) of the directed motion.

Based on these Equations, motion-characteristic parameters such as D , v or α can be determined from the variations of MSD with time lag t , and that is exactly what we get from tracking particles. The x , y -coordinates generated by particle tracking are used to calculate MSD. In our experimental setup, each acquisition was 1400 frames with 0.2 s exposure time and no delay. For MSD calculation, a window segment (or sub-trajectory) length of 100 frames or 20 s is chosen and shifted along the whole trajectory track with 0.2 s (1 frame) step size so that each trajectory has a total of 1300 sub-trajectories. One set of time-lag-dependent MSD values is calculated from each sub-trajectory. Plotting these sub-trajectories versus the time lag results in an MSD curve from which the characteristic diffusion coefficient D value can be obtained. For the experiment I have observed, with about 30 to 60 tracked particles, the total number of MSD curves, or (sub)trajectories, per population can be thousands to tens thousand, supposed to be efficient to minimize the uncertainty.

Fig. 3.5 shows the average MSD curves of different populations (MOONs in macrophage cells without toxin addition, MOONs in cells with toxin addition, and simulated MOONs with random motions). These characteristic curves are the average of all sub-trajectories of the same population. The curve generated from simulated Brownian motion in **Fig. 3.5a** is linear, as expected for the normal diffusive motion. The curve of motion in cells without toxin treatment is slightly bent from linear, indicating a small portion of directed transport (**Fig. 3.5b**). On the other hand, **Fig 3.5c** shows confined diffusion, where MSD reaches saturation immediately, implying a very limited motion and can be explained by the ATP-based motion inhibitors azide and 2-deoxy-D-glucose.

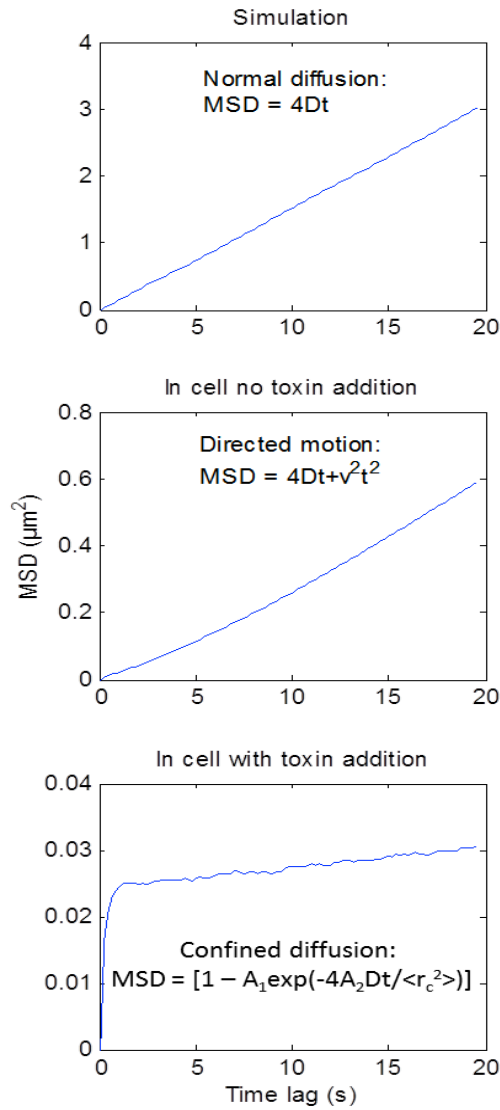


Fig. 3.5. MSD curves of simulated Brownian motion (a), motion in cells with no toxin addition (b), and motion in cells with toxin (NaN₃ + 2-deoxy-D-glucose) addition (c).

The next step after MSD calculation is fitting. The fitting function basically finds all the coefficients to present the relationship between MSD and time lag t . To compare to related studies (125, 127), both Equation 3 and 4 were used for fitting to find the

diffusion coefficient D , velocity v , and exponent α . **Table 3.1** shows these values in cells not treated with toxin. Compared to a similar experiment on HeLa cells of Holzbaur and colleagues (127), which has $\alpha = 0.32 \pm 0.09$ and $D = 0.006 \pm 0.001$, our studied population is more diffusive with significantly higher values of both α (0.71 ± 0.43) and D (0.022 ± 0.027). It is worth noting that the D values of my data obtained from both fittings (D_α from Equation 3 and D_v from Equation 4) are the same.

Table 3.1. Motion characterization: D , v and α .

	α		D_α ($\mu\text{m}^2/\text{s}$)		v ($\mu\text{m}/\text{s}$)		D_v ($\mu\text{m}^2/\text{s}$)	
	Average	SD	Average	SD	Average	SD	Average	SD
Cells with no toxin added	0.71	0.43	0.022	0.027	0.025	0.048	0.022	0.027

The obtained α values were then used to classify the types of motions. **Fig. 3.6** shows histograms of α resulting from fitting MSD data of 36 particles in each of the three populations: in cells with toxin addition, in cells not adding toxin, and simulated random motions. While simulated particles resulted in Gaussian distribution of diffusive behavior and toxin addition caused a confined motion the in cells without toxin histogram showed a multimodal distribution (multiple peaks), suggesting there were different types of motion co-occurring in the population. The thresholds to separate the three types, confined, diffusive and directed motions were chosen based on the normal distribution of the simulated motions as $\alpha_1 = \bar{\alpha} - 3 \sigma = 0.61$ and $\alpha_2 = \bar{\alpha} + 3 \sigma = 1.35$, where $\bar{\alpha}$ is the average of α and σ is its standard deviation. Using these thresholds, the coefficients generated from the fitting and also the MSD values can be separated into groups. Counting the total sub-trajectories of each group gives the percentage (over all sub-

trajectories) of each motion type. The variation of this percentage value among 6 groups of 6 particles is shown in **Table 3.2**.

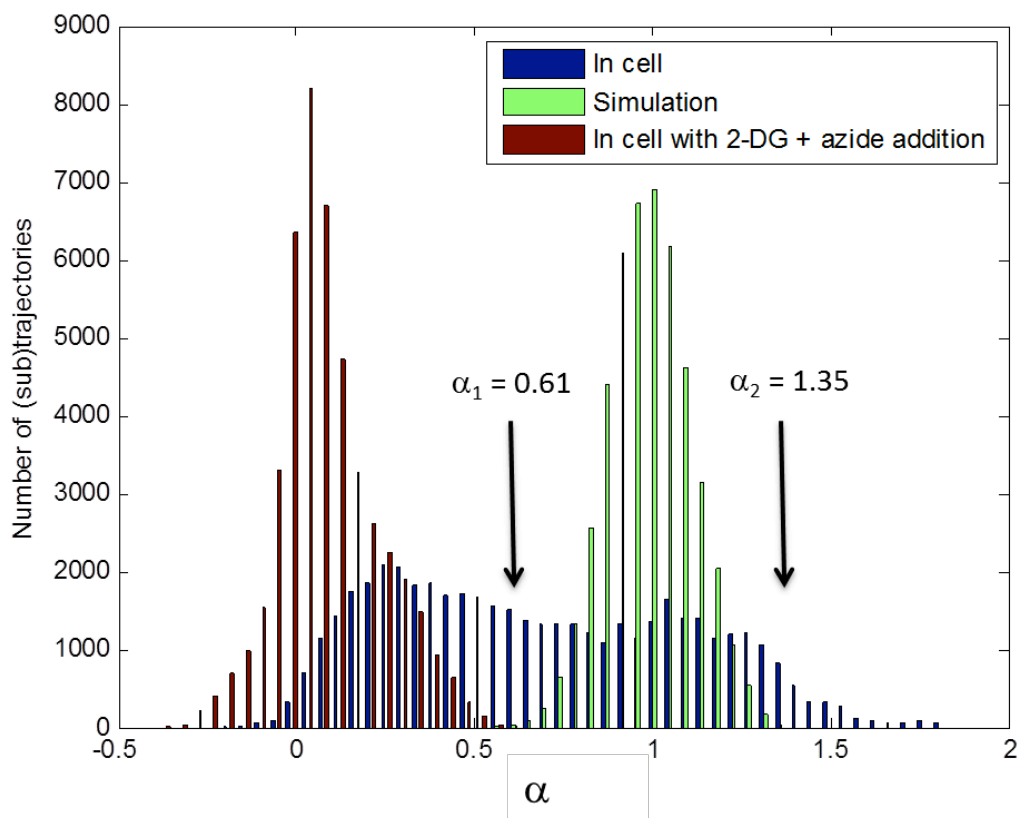


Fig. 3.6. Motion classification based on α . The α histograms of three populations of 36 particles (total of 46800 sub-trajectories).

In the toxin addition population, the particles don't show any normal diffusion (0%) or directed motion (0%) (**Table 3.2**). Compared to the corresponding results of Holzbaur and colleagues study on HeLa cells (127), our cellular control population showed to be more dynamic with higher percentages of diffusive (48% versus 39%) and directed (7% versus 2%) behaviors, and a lower percentage of confined motions (45%

versus 59%) (**Table 3.2**). In conclusion, the quantitative analysis based on MSD can be a reliable tool to evaluate cytotoxicity.

Table 3.2. Motion characterization: percentage of confined, diffusive and directed motion.

	Confined diffusion	Normal diffusion	Directed motion
Cells with no toxin addition	45 ± 19%	48 ± 16%	7 ± 4%
Cells with toxin addition	100% ± 0%	0% ± 0%	0% ± 0%
Simulated particles	0% ± 0%	100% ± 0%	0% ± 0%

Conclusions and Future Work

Intracellular transport mechanisms can be elucidated by using rotational and translational tracking of single anisotropic-optical tracers. Moreover, observation over an ensemble of MOON tracers provides the global characteristics of that population and can be used to distinguish different populations. The potential of applying this rotation and translation tracking system to study cytotoxicity was confirmed using intracellular-transport-inhibitory cytoskeletal drugs.

CHAPTER FOUR

SUMMARY AND FUTURE WORK

In summary, this research explored the potential of anisotropic optical tracers together with rotational and translational SPT technique in studying biophysical processes. Anisotropic optical tracers have asymmetric optical properties so that their intensity is orientation-dependent. Fabrication of these tracers from spherical fluorescent probes is quite simple. Basically, a thin metal layer is vapor deposited on one hemisphere of these probes. Tracking the rotation and translation of these tracers using fluorescent microscopy in a gel can report the appearance of an enzyme or a chemical that causes viscosity changes in the gel. The same system also can be used to study dynamic processes such as intracellular transport in macrophages in which tracers are phagocytosed into the phagosome and transported by cellular protein motors. The intracellular transport behavior can be employed to evaluate cytotoxicity as well. This is the first time rotational and translational SPT is used to study cytotoxicity.

For cell work, the most important factor to obtain reproducible results is the consistency of experimental conditions between experimental batches of cells such as the cell confluence when imaging. Improvements can also be made in: reducing the exposure time and the observation time to minimize the effect of illuminating light on cell health; increasing the temporal resolution for higher tracking accuracy; and optimizing the tracking algorithm for a faster, more efficient and more accurate tracking. With these improvements, we expect to be able to build a calibration curve from varied

concentrations of particulate matters. The curve will establish our first step toward the quantitative evaluation of particulate matter cytotoxicity.

Not only for intracellular processes, our rotational and translational SPT system can also have its use in investigating the interactions or processes on cell membrane as presented in Appendix B. Here a $\sim 4 \mu\text{m}$ MagMOON, made from a Fe_3O_4 core and coated with Au on one hemisphere, was tracked while being modulated by an external magnetic field. Its binding to the cell membrane was detected by the magnetic modulation amplitude depletion. Due to its large size ($4 \mu\text{m}$) and strong magnetism, this MagMOON caused mechanical stress on the bound cell since it still rotated, although with smaller amplitude than that before binding, in response to the external magnetic field. Eventually, the cell ruptured and the MagMOON was released and showed strong modulation again. This work suggests the potential of using our method to study processes on cell membranes.

Another future direction is utilizing different tracer types, including size and shape variations. Our group continues to try applying smaller optical magnetic tracers (200 nm or less) so that they can be easily manipulated by an external magnetic field after being phagocytosed. Beside spherical probes, Zhang from our group also successfully synthesized (several nanometer in diameter and a couple of hundred nanometer long) silver nanoribbons (81, 137) that may be good candidates for studying biophysical processes using rotational SPT technique based on their anisotropic optical properties.

APPENDICES



Magnetically modulated single particle tracking as a tool to study cytotoxicity of airborne nanoparticles

KhanhVan T. Nguyen¹, Lawrence P. Fernando¹, Kenneth A. Christensen¹, Winfried Möller², Jeffrey N. Anker^{1*}

¹ Chemistry Department, Clemson University, Clemson, SC 29634, USA

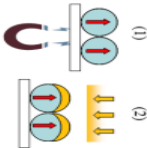
² Institute For Lung Biology And Disease, Helmholtz Zentrum München - GmbH, Neuherberg D-85764, Germany

 *anker@clemson.edu

Abstract

Macrophages are the primary defence cells in the lung responsible for uptake and clearance of foreign particles, debris, viruses and bacteria. These biophysical processes can be studied by tracking the trajectory of individual particles as they diffuse through the medium, bind to the cell surface, and are internalized. However, it is challenging to track translation in situ at low magnification. We have developed a novel technique to track adhesion, release, and intracellular transport of phycoerythrin magnetically modulated optical nanoparticles (MagMOONS). These MagMOONS are micron sized tracer particles with one hemisphere coated by gold creating an orientation-dependent scattering and fluorescence signal. The particles align with an external magnetic field and blink when they rotate in response to a rotating magnetic field. Tracking rotational transport via intensity changes allows analysis of many particles simultaneously even at low magnification. In this study, we track the MagMOONS blinking signal as they non-specifically bind onto J774A macrophage cell membrane, and then are released during membrane rupture.

Preparation and Characterization of MagMOONS



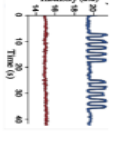
(1) Magnetize micron size Fe₃O₄/γ-Fe₂O₃ microspheres on a glass cover-slip.

(2) Vapor deposit a thin layer of metal (Au, Ag, Al) on one hemisphere of the particles.

SEM image of a MagMOON synthesized by Muller, made by vapor depositing Au onto one hemisphere of an Fe₃O₄ microsphere. The arrow points to the gold-coated hemisphere.

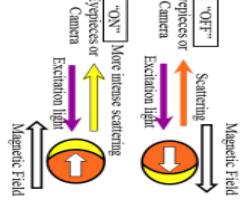
The ~ 0.5 mT magnetic field is rotated 180° "on" and "off" every 5 seconds. Acquisition is taken under bright field and dark field microscopy and the light intensity of the observed particles is recorded versus time.

For a better modulation, a three-dimensional coil can be used to generate a magnetic field of ~ 1 mT at the sample stage center. The field generation is controlled by a Labview program.



Scattering intensity vs. time of a 1.44 μm MagMOON (blue) and background (red) in a pulsed magnetic field.

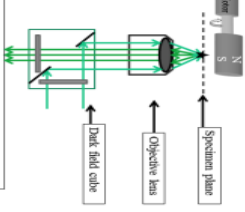
Principle of MagMOON's



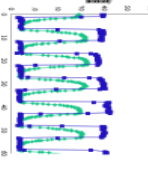
MagMOONS appear to blink, "OFF" when the light comes to the non-gold-coated hemi-sphere, and "ON" as the light faces the metal-coated site, as they rotate in response to rotating magnetic fields, enabling separation of the particles from un-modulated backgrounds.

Aster, N.; Espinosa, R. "Magnetically Modulated Optical Nanoparticles." *Applied Physics Letters* 92: 1011-1014, 2008

MagMOON Viscometer



Intensity change of a modulated MagMOON in glycerol/water solution of 95% (green) and 75% (blue square wave) indicates the ability of using MagMOONS as viscometers.

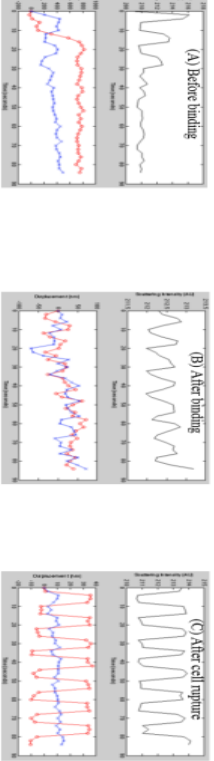


Acquisition is taken under bright field and dark field microscopy and the light intensity of the observed particles is recorded versus time.

MagMOONS on Macrophages' Surface

Magnetic modulation of 3.9 μm MagMOON particle (Fe₃O₄/Au) on a J774A1 macrophage's surface

Tracking the intensity of a magnetically modulated moon-shaped particle provides both the particle trajectory and its intensity change. The intensity change in response to the magnetic modulation reflects particle's rotational motion. When translational motion is difficult to track, e.g. at low magnification or in a moving system, information of particle rotation still can be obtained from its intensity change. Figure (A), (B) and (C) show that tracking intensity and x and y-displacement reveals information of different biophysical processes.



(A) Before binding
(B) After binding
(C) After cell rupture

Plots of scattering intensity (black -), x-displacement (red ○) and y-displacement (blue x) versus time of a magnetically modulated particle before (A) and after (B) it binds to J774A macrophage and after the cell membrane ruptures (C). Particle: 3.9 μm Fe₃O₄/hemispherically coated with 50 nm gold. The ~ 0.5 mT external magnetic field is rotated 180° "on" and "off" every 5 seconds.

(A) Before MagMOON attaches to macrophage surface there is intense modulation which decreases when the particle attaches to the surface. Particle moves ~ 100 μm/s in cell medium. After landing on cell surface, the speed of movement reduces by from a half to no third.

(B) minimal modulation after 1 hour the particle attaches on macrophage surface. Despite being small, the magnitude modulation can be seen observing intensity regulation.

(C) restoration of modulation after the cell membrane ruptures. This modulation can be seen clearly at the x-displacement plot. It also shows that the modulation is more along x rather than y coordinate.

Conclusion and Future Work

- This study demonstrated that the rotation and translation of single MagMOONS particles can be tracked simultaneously.
- Magnetically modulated single particle tracking can also be applied to identify binding event and binding/unbinding rates.
- Future work will include the investigation of the uptake, transport and clearance in macrophage and the effect of nanoparticles on those processes.



Acknowledgement

This work was supported by the South Carolina Research Authority NSF grant 2002-29910-040056, and a Vietnam Education Foundation (VEF) fellowship to XVTN.



Appendix C

Matlab Script for Particle Tracking

-----PARTICLE TRACKING-----

```
function [MxT, MyT, meanItotal, maxItotal, meanI0, meanIBG, ameanBG, CIntT] = ptrack_V35(n0ofparticles, framerate, frns, sw1, sw2, XY, thresh)
```

```
%This program tracks blinking particles based on their centroids.  
%Find the centroid position within a specific region in the first  
%frame, then continue finding it within a limited area around the first  
%point.
```

```
Coordinations x,y of the particles need to be put in XY matrix ahead.  
%the numberofparticles needs to be n+1 since you have the background at  
the end.
```

```
%n0ofparticles: number of particles to track that was listed in XY  
matrix (including the background point)
```

```
%framerate: frame/sec; frns: 1:n;
```

```
%sw1: stepwise to calculate mean and max; sw2: stepwise of tracking  
area;
```

```
% XY: matrix of coordinations of the ROI, chosen at first frame.
```

```
% Thresh: the threshold chosen that is higher than background but  
better be lower than particle intensity when it is dark.
```

```
% OPEN FILE
```

```
[fn pn]=uigetfile('*.tif');
```

```
cd(pn);
```

```
% MAIN BODY
```

```
% Display running progress (number of particles)
```

```
for j=1:n0ofparticles-1,  
display particle; display(j)
```

```
[x]=XY(j,1);
```

```
[y]=XY(j,2);
```

```
% Display running progress (every 100 frames)
```

```
for i=1:size(frns,2),  
if rem(i,100)==0, display(i); end;
```

```
I(:,:,:)=imread(fn,frns(i)); %read image i
```

```
if i==1,
```

```
%figure; imshow(I*256);
```

```
J2=(I(y-sw2:y+sw2,x-sw2:x+sw2));
```

```
%figure; imshow(J2*256);
```

```

                [Cx(i), Cy(i), CInt(i)]=centroid(J2,thresh); %calculate
centroid
                Cx(i)=Cx(i)+(x-sw2)-1;
                Cy(i)=Cy(i)+(y-sw2)-1;
            else %after the first frame
                J2=(I(round(Cy(i-1))-sw2:round(Cy(i-1))+sw2, round(Cx(i-1))-sw2:round(Cx(i-1))+sw2));

                [Cx(i), Cy(i), CInt(i)]=centroid(J2,thresh); %calculate
centroid

                Cx(i)=Cx(i)+round(Cx(i-1))-sw2-1;
                Cy(i)=Cy(i)+round(Cy(i-1))-sw2-1;
            end; %end find centroid if frame i=1 or not

% CALCULATION OF MEAN AND MAX INTENSITY

                meanI(i)=mean(mean(I(round(Cy(i))-sw1:round(Cy(i))+sw1,round(Cx(i))-sw1:round(Cx(i))+sw1)));
                maxI(i)=max(max(I(round(Cy(i))-sw1:round(Cy(i))+sw1,round(Cx(i))-sw1:round(Cx(i))+sw1)));

end; %for each frame
    meanItotal(:,j)=meanI;
    maxItotal(:,j)=maxI;

    MxT(:,j)=Cx;
    MyT(:,j)=Cy;
    CIntT(:,j)=CInt;
end;

% TRACKING BACKGROUND REFERENCE POINT

for p=1:size(frns,2),
    I(:,:,:)=imread(fn,frns(p));
    J3=I(XY(end,2)-10:XY(end,2)+10,XY(end,1)-10:XY(end,1)+10);
    [Cx0(p), Cy0(p), CInt0(p)]=centroid(J3,100); %calculate centroid
    meanI0(p)=mean(mean(I(round(Cy0(p))-sw1:round(Cy0(p))+sw1,round(Cx0(p))-sw1:round(Cx0(p))+sw1)));
    maxI0(p)=max(max(I(round(Cy0(p))-sw1:round(Cy0(p))+sw1,round(Cx0(p))-sw1:round(Cx0(p))+sw1)));
end;

% AUTOCORRELATION CALCULATION

s=size(frns,2); %s is number of frames in movie.
for k=1:nofparticles-1, %for each particle k
    meanIBG(:,k)=meanItotal(:,k)-meanI0(:,1);
    ameanBG(:,k)=auto(meanIBG(:,k),s-2);
end;
amax(:,j)=auto(maxItotal(:,j),size(frns,2)-2);
amean=auto(meanItotal,i+(k-1)*period);
-----END-----

```

Appendix D

Matlab Script for MSD Calculation

```
-----MSD CALCULATION-----
function [msdr, msdrA]=MSD_no_var (MxT,MyT,n0ofparticles,segL,c,frns,s)

%This function calculates Mean Squared Displacement for all
trajectories of
%all particles within a population.

% Each acquisition is 1400 frames with 0.2 s exposure time and no
delay.
% For MSD calculation a window segment (or sub-trajectory) length
(segL) of 100 frames or 20 s is chosen and shifted along the whole
trajectory track with 0.2 s (1 frame) step size. So each trajectory has
total of 1300 sub-trajectories.
% One set of time lag-dependent MSD values is calculated from each sub-
trajectory.
% MSD was taken over all 1400 frames, not cutting into smaller tracks
(frns = s = 1400, scanning step c = 1 unit)

% msdr: mean squared displacement in r (both x and y movement)
% msdrA: mean of all msdr
% s is number of frames in movie.
%segL: length of each segment; here all segments have equal length;
scan a window of "segL" length through the whole movie length

n=n0ofparticles;
msdr=zeros(segL-1,n*floor((frns-s)/s)*floor((s-segL)/c));%create zero
matrix

for p=1:n0ofparticles,
    display(p);

    for w=1:floor(frns/s),%w = number of sections of s frames from
original Mx, My
        qa=(w-1)*s;
        for ns=1:floor((s-segL)/c), %ns = n0ofsegments;
            q=(ns-1)*c; % the position in the whole movie
            for m=1:segL-1,%calculation for each segment

                %displacement vector
                deltaX=MxT(m+q+qa:segL+q+qa,p)-MxT(1+q+qa:segL-
m+1+q+qa,p);
                deltaY=MyT(m+q+qa:segL+q+qa,p)-MyT(1+q+qa:segL-
m+1+q+qa,p);
```

```
        %squared displacement vector
        sdx=deltaX.^2;
        sdy=deltaY.^2;
        sdr=sdX+sdY;

        %mean squared displacement
        msdr(m,ns,p)=sum(sdr)/length(sdr);
    end;
end;
end;
msdrA=msdr(1:segL-1,:);
```

-----END-----

Appendix E

Matlab Script for Motion Classification

-----MOTION CLASSIFICATION-----

```
%This is a sample script for MSD analysis of inputs Mx140 and My140.
Mx140,My140 size is (1400,58) <1400 frames, 58 particles>
%Outputs include percentages of directed motion, normal diffusion and
%confined diffusion over all (sub)trajectories; mean values in all and
in each group of motion of diffusion coefficients D, exponent alpha,
and velocity v.
```

```
%I. MSD CALCULATION
```

```
%1. Load Mx140, My140
```

```
%2. Change unit from pixel to um:
```

```
Mx140um=Mx140*0.43;My140um=My140*0.43;
```

```
%3. Calculate MSD by the script MSD_no-var: for nd140 (in cell no
toxin), 58 particles, segL = 100; take MSD over all 1400 frames, not
cutting into smaller tracks (frns = s = 1400)
```

```
[msdr140um]=MSD_no_var(Mx140um,My140um,58,100,1,1400,1400);
```

```
%Result of MSD calculation above is MSD as a function of time lag from
1 frame to 99 frames; for all particles and all trajectories of 100
frames in length.
```

```
%-----
```

```
%II. FITTING
```

```
t=[0.2:0.2:1]';
```

```
a=msdr140um(2:6,:);
```

```
total=size(a,2);
```

```
xdata=t;
```

```
%1. Fitting the normal and abnormal (alpha <1) motion (Equation 4)
```

```
%  $y = x(1)*tx(2)$  , whereas  $x(1) = 4D$  and  $x(2)=\alpha$ ;  $y=MSD$ ,  $t=time\ lag$ 
```

```
% Replace t with xdata, y with F,
```

```
% $F=@(x,xdata)x(1)*xdata.^x(2)$  ;
```

```
%So just need to assign xdata as time lag vector t; and y as MSD
```

```
for i=1:total, x(1)=0.0034;x(2)=1; y=a(:,i);
```

```
F=@(x,xdata)x(1)*xdata.^x(2) ;
```

```
[x,resnorm,~,exitflag,output] = lsqcurvefit(F,x,t,y); xtest7(:,i)=x;
```

```
end;
```

```
%2. Fitting the directed motion (velocity). Equation 3
```

```
% $y = x(1)*t + x(2)^2 *t^2$ , whereas  $x(1) = 4D$  and  $x(2)=\sim v^2$ ;  $y=MSD$ ,
```

```
 $t=time\ lag$ 
```

```
% Replace t with xdata, y with F,
```

```
% $F=@(x,xdata)x(1)*xdata+x(2)*xdata.^2$ ;
```

```
%So just need to assign xdata as time lag vector t; and y as MSD
```

```
for i=1:total, x(1)=0.0034;x(2)=1; y=a(:,i);
```

```
F=@(x,xdata)x(1)*xdata+x(2).^2*xdata.^2;
```

```
[x,resnorm,~,exitflag,output] = lsqcurvefit(F,x,t,y);
```

```
xtest6(:,i)=x;
```

```
end;
```



```

%-----
%checking hist of alpha to choose thresholds c1 and c2
figure; hist(xtest6(2,:),50);
c1=0.61; c2=1.35;
%-----

%III. GROUPING MSD AND D, ALPHA, (VELOCITY)
%Grouping MSD after motion classification and % calculation Normal
fitting Alpha (the same for both models)
%Make sure only needed values are present, to avoid same name conflict;
input NEED: msdr140um; xtest7; c1;c2;
a2=msdr140um(1:99,:);
k=0;k1=0;k2=0;k3=0;
for i=1:size(a2,2),
if xtest7(2,i)> c2, %classify sliding
xslide(:,k1+1)=xtest7(:,i);
MSDslide(:,k1+1)=a2(:,i); k1=k1+1;
else
if xtest7(2,i)<c1, %classify immotile
xim(:,k3+1)=xtest7(:,i);
MSDim(:,k3+1)=a2(:,i); k3=k3+1;
else %remaining is diffusive
xdif(:,k2+1)=xtest7(:,i);
MSDdif(:,k2+1)=a2(:,i); k2=k2+1;
end;end;end;

%-----
%REPEAT FOR THE DIRECTED MOTION MODEL WITH xtest6
%-----

%IV. CALCULATION
%Generate percentage, mean and std of Alpha and Diffusion coefficient
pcim=size(xim)/(size(xslide)+size(xim)+size(xdif))
pcslide=size(xslide)/(size(xslide)+size(xim)+size(xdif))
pcdif=size(xdif)/(size(xslide)+size(xim)+size(xdif))
meanD140=mean(xtest6(1,:))
stdD140=std(xtest6(1,:))
meanD140im=mean(xim(1,:))
stdD140im=std(xim(1,:))
meanD140dif=mean(xdif(1,:))
stdD140dif=std(xdif(1,:))
meanD140slide=mean(xslide(1,:))
stdD140slide=std(xslide(1,:))

meanA140=mean(xtest6(2,:))
stdA140=std(xtest6(2,:))
meanA140im=mean(xim(2,:))
stdA140im=std(xim(2,:))
meanA140dif=mean(xdif(2,:))
stdA140dif=std(xdif(2,:))
meanA140slide=mean(xslide(2,:))
stdA140slide=std(xslide(2,:))

```

-----END-----

Appendix F License Agreement



RightsLink®

[Home](#)[Account Info](#)[Help](#)

Title: Detecting de-gelation through tissue using magnetically modulated optical nanoprobes (MagMOONs)
Author: K.V.T. Nguyen, Jeffrey N. Anker
Publication: Sensors and Actuators B: Chemical
Publisher: Elsevier
Date: 15 December 2014

Logged in as:
Khanh Van Nguyen

[LOGOUT](#)

Copyright © 2014 Elsevier B.V. All rights reserved.

Order Completed

Thank you very much for your order.

This is a License Agreement between Khanh Van T Nguyen ("You") and Elsevier ("Elsevier"). The license consists of your order details, the terms and conditions provided by Elsevier, and the [payment terms and conditions](#).

[Get the printable license.](#)

License Number	3679460808900
License date	Jul 31, 2015
Licensed content publisher	Elsevier
Licensed content publication	Sensors and Actuators B: Chemical
Licensed content title	Detecting de-gelation through tissue using magnetically modulated optical nanoprobes (MagMOONs)
Licensed content author	K.V.T. Nguyen, Jeffrey N. Anker
Licensed content date	15 December 2014
Licensed content volume number	205
Licensed content issue number	n/a
Number of pages	9
Type of Use	reuse in a thesis/dissertation
Portion	full article
Format	electronic
Are you the author of this Elsevier article?	Yes
Will you be translating?	No
Title of your thesis/dissertation	Tracking anisotropic optical tracer to study biophysical processes and cytotoxicity
Expected completion date	Aug 2015
Estimated size (number of pages)	95
Elsevier VAT number	GB 494 6272 12
Permissions price	0.00 USD
VAT/Local Sales Tax	0.00 USD / 0.00 GBP
Total	0.00 USD

[ORDER MORE...](#)[CLOSE WINDOW](#)

Copyright © 2015 Copyright Clearance Center, Inc. All Rights Reserved. [Privacy statement](#). [Terms and Conditions](#).
Comments? We would like to hear from you. E-mail us at customer@copyright.com

REFERENCES

1. G. Oberdörster, A. Maynard, K. Donaldson, V. Castranova, J. Fitzpatrick *et al.*, *Particle and Fibre Toxicology* **2**, 8 (2005).
2. M. J. Wade, L. E. Lipkin, R. W. Tucker, A. L. Frank, *Nature* **264**, 444 (1976).
3. A. M. Knaapen, P. J. A. Borm, C. Albrecht, R. P. F. Schins, *International Journal of Cancer* **109**, 799 (2004).
4. T. J. Brunner, P. Wick, P. Manser, P. Spohn, N. Robert *et al.*, *Environmental science & technology* **40**, 4374 (2006).
5. A. Valavanidis, T. Vlachogianni, K. Fiotakis, S. Loridas, *International journal of environmental research and public health* **10**, 3886 (2013).
6. N. A. M. Howlader N, Krapcho M, Garshell J, Miller D, Altekruse SF, Kosary CL, Yu M, Ruhl J, Tatalovich Z, Mariotto A, Lewis DR, Chen HS, Feuer EJ, Cronin KA (eds), National Cancer Institute, Bethesda, MD, (2014).
7. C. A. Pope III, R. T. Burnett, M. J. Thun, E. E. Calle, D. Krewski *et al.*, *Jama* **287**, 1132 (2002).
8. N. Hanagata, F. Zhuang, S. Connolly, J. Li, N. Ogawa *et al.*, *ACS nano* **5**, 9326 (2011).
9. K. Donaldson, F. Murphy, R. Duffin, C. Poland, *Particle and Fibre Toxicology* **7**, 5 (2010).
10. Y.-N. Chang, M. Zhang, L. Xia, J. Zhang, G. Xing, *Materials* **5**, 2850 (2012).
11. M.-F. Song, Y.-S. Li, H. Kasai, K. Kawai, *Journal of clinical biochemistry and nutrition* **50**, 211 (2012).
12. M. Xu, D. Fujita, S. Kajiwarra, T. Minowa, X. Li *et al.*, *Biomaterials* **31**, 8022 (2010).
13. Z. Wang, N. Li, J. Zhao, J. C. White, P. Qu *et al.*, *Chemical research in toxicology* **25**, 1512 (2012).
14. J. R. Tennant, *Transplantation* **2**, 685 (1964).
15. W. Strober, *Current protocols in immunology* **21**, A. 3B. 1 (2001).
16. A. Krishan, *The Journal of cell biology* **66**, 188 (1975).
17. D. B. Mitchell, K. S. Santone, D. Acosta, *Journal of tissue culture methods* **6**, 113 (1980).
18. T. Decker, M.-L. Lohmann-Matthes, *Journal of immunological methods* **115**, 61 (1988).
19. T. Mosmann, *Journal of immunological methods* **65**, 55 (1983).
20. G. Malich, B. Markovic, C. Winder, *Toxicology* **124**, 179 (1997).
21. Y. Maehara, H. Anai, R. Tamada, K. Sugimachi, *European Journal of Cancer and Clinical Oncology* **23**, 273 (1987).
22. D. Cohen, *Science* **180**, 745 (1973).
23. D. Cohen, S. F. Arai, J. D. Brain, *Science* **204**, 514 (1979).
24. A. P. Freedman, and S. E. Robinson, N. Y. Walter de Gruyter Berlin, Ed. (1981), pp. 489-495.

25. I. Nemoto, *IEEE Transactions on Biomedical Engineering* **29**, 745 (1982).
26. P. A. Valberg, J. P. Butler, *Biophysical Journal* **52**, 537 (1987).
27. W. Stahlhofen, W. Möller, *Radiation and Environmental Biophysics* **32**, 221 (1993).
28. W. Möller, S. Takenaka, M. Rust, W. Stahlhofen, J. Heyder, *Journal of Aerosol Medicine* **10**, 173 (1997).
29. W. Möller, I. Nemoto, T. Matsuzaki, T. Hofer, J. Heyder, *Biophysical journal* **79**, 720 (2000).
30. W. Möller, T. Hofer, A. Ziesenis, E. Karg, J. Heyder, *Toxicology and applied pharmacology* **182**, 197 (2002).
31. B. N. G. Giepmans, S. R. Adams, M. H. Ellisman, R. Y. Tsien, *Science* **312**, 217 (2006).
32. H. Qian, M. P. Sheetz, E. L. Elson, *Biophysical journal* **60**, 910 (1991).
33. R. D. Vale, T. S. Reese, M. P. Sheetz, *Cell* **42**, 39 (1985).
34. J. Gelles, B. J. Schnapp, M. P. Sheetz, *Nature* **331**, 450 (1988).
35. A. Yildiz, P. R. Selvin, *Accounts of chemical research* **38**, 574 (2005).
36. S. Courty, C. Luccardini, Y. Bellaiche, G. Cappello, M. Dahan, *Nano letters* **6**, 1491 (2006).
37. M. J. Saxton, K. Jacobson, *Annual review of biophysics and biomolecular structure* **26**, 373 (1997).
38. D. J. Stephens, V. J. Allan, *Science* **300**, 82 (2003).
39. X. Michalet, F. F. Pinaud, L. A. Bentolila, J. M. Tsay, S. J. J. L. Doose *et al.*, *science* **307**, 538 (2005).
40. L. P. Fernando, P. K. Kandel, J. Yu, J. Mcneill, P. C. Ackroyd *et al.*, *Biomacromolecules* **11**, 2675 (2010).
41. J. Suh, M. Dawson, J. Hanes, *Advanced drug delivery reviews* **57**, 63 (2005).
42. S. S. Benjamin, M. E. Laura, B. A. Daniel, S. S. Jung, H. Justin, *Advanced Drug Delivery Reviews* **in press**, (2015).
43. N. Ruthardt, D. C. Lamb, C. Bräuchle, *Molecular therapy* **19**, 1199 (2011).
44. Y. Gu, J. W. Ha, A. E. Augspurger, K. Chen, S. Zhu *et al.*, *Nanoscale* **5**, 10753 (2013).
45. E. Toprak, J. Enderlein, S. Syed, S. A. Mckinney, R. G. Petschek *et al.*, *Proceedings of the National Academy of Sciences* **103**, 6495 (2006).
46. G. Wang, W. Sun, Y. Luo, N. Fang, *J Am Chem Soc* **132**, 16417 (2010).
47. Y. Gu, G. Wang, N. Fang, *ACS nano* **7**, 1658 (2013).
48. W. Sun, Y. Gu, G. Wang, N. Fang, *Analytical chemistry* **84**, 1134 (2011).
49. C. J. Behrend, J. N. Anker, B. H. Mcnaughton, M. Brasuel, M. A. Philbert *et al.*, *The Journal of Physical Chemistry B* **108**, 10408 (2004).
50. C. J. Behrend, J. N. Anker, B. H. Mcnaughton, R. Kopelman, *Journal of magnetism and magnetic materials* **293**, 663 (2005).
51. S. M. Anthony, M. Kim, S. Granick, *Langmuir* **24**, 6557 (2008).
52. K. Y. Lee, D. J. Mooney, *Progress in polymer science* **37**, 106 (2012).
53. Y. Li, J. Rodrigues, H. Tomas, *Chemical Society Reviews* **41**, 2193 (2012).

54. H. H. Tønnesen, J. Karlsen, *Drug development and industrial pharmacy* **28**, 621 (2002).
55. S. Brulé, M. Levy, C. Wilhelm, D. Letourneur, F. Gazeau *et al.*, *Advanced Materials* **23**, 787 (2011).
56. L. A. Wells, H. Sheardown, *European journal of pharmaceutics and biopharmaceutics* **65**, 329 (2007).
57. S. Zhang, H. Niu, Y. Cai, Y. Shi, *Analytica chimica acta* **665**, 167 (2010).
58. C. Chang, B. Duan, L. Zhang, *Polymer* **50**, 5467 (2009).
59. D. Queen, H. Orsted, H. Sanada, G. Sussman, *International wound journal* **1**, 59 (2004).
60. J. A. Rowley, D. J. Mooney, *Journal of biomedical materials research* **60**, 217 (2002).
61. M. D. Krebs, E. Salter, E. Chen, K. A. Sutter, E. Alsberg, *Journal of Biomedical Materials Research Part A* **92**, 1131 (2010).
62. S. Levenberg, J. Rouwkema, M. Macdonald, E. S. Garfein, D. S. Kohane *et al.*, *Nature biotechnology* **23**, 879 (2005).
63. A. J. Thornton, E. Alsberg, M. Albertelli, D. J. Mooney, *Transplantation* **77**, 1798 (2004).
64. F. Gu, B. Amsden, R. Neufeld, *Journal of Controlled Release* **96**, 463 (2004).
65. W. Ostwald, *Transactions of the Faraday Society* **29**, 1002 (1933).
66. R. Lapasin, S. Pricl, in *Rheometry*, Eds. (Springer, 1995), pp. 495-578.
67. A. R. Bausch, W. Möller, E. Sackmann, *Biophysical journal* **76**, 573 (1999).
68. W. Möller, W. G. Kreyling, M. Kohlhäufel, K. Häussinger, J. Heyder, *Journal of magnetism and magnetic materials* **225**, 218 (2001).
69. G. D. Ehrlich, P. Stoodley, S. Kathju, Y. Zhao, B. R. Mcleod *et al.*, *Clinical orthopaedics and related research* **437**, 59 (2005).
70. N. Belmiloud, I. Dufour, L. Nicu, A. Colin, *5th IEEE Conference on Sensors* 753 (2006).
71. A. Agoston, F. Keplinger, B. Jakoby, *Sensors and Actuators A: Physical* **123-124**, 82 (2005).
72. F. H. C. Crick, A. F. W. Hughes, *Experimental Cell Research* **1**, 37 (1950).
73. B. H. Mcnaughton, R. R. Agayan, R. Clarke, R. G. Smith, R. Kopelman, *Applied Physics Letters* **91**, 224105 (2007).
74. R. Elbez, B. H. Mcnaughton, L. Patel, K. J. Pienta, R. Kopelman, *PLoS ONE* **6**, e28475 (2011).
75. A. Tokarev, B. Kaufman, Y. Gu, T. Andruk, P. H. Adler *et al.*, *Applied Physics Letters* **102**, 033701 (2013).
76. I. Sinn, T. Albertson, P. Kinnunen, D. N. Breslauer, B. H. Mcnaughton *et al.*, *Analytical Chemistry* **84**, 5250 (2012).
77. K. Paivo, S. Irene, H. M. Brandon, W. N. Duane, A. B. Mark *et al.*, *Biosensors and Bioelectronics* **26**, 2751 (2011).
78. J. N. Anker, C. J. Behrend, H. Huang, R. Kopelman, *Journal of magnetism and magnetic materials* **293**, 655 (2005).
79. S. Koichi, T. Koji, K. Yuji, *Appl. Opt.* **44**, 2154 (2005).

80. V. Ntziachristos, *Nat Meth* **7**, 603 (2010).
81. Z. Yang, H. Qian, H. Chen, J. N. Anker, *Journal of colloid and interface science* **352**, 285 (2010).
82. Y. Nan, E. C. Adam, *Opt. Express* **18**, 25461 (2010).
83. J. Haegele, S. Biederer, H. Wojtczyk, M. Gräser, T. Knopp *et al.*, (2013), pp. 1761—1767.
84. T. Y. Wong, L. A. Preston, N. L. Schiller, *Annual Review of Microbiology* **54**, 289 (2000).
85. J. N. Anker, R. Kopelman, *Applied physics letters* **82**, 1102 (2003).
86. C. J. Behrend, J. N. Anker, R. Kopelman, *Applied physics letters* **84**, 154 (2004).
87. G. Peter, *Carbohydrate Polymers* **8**, 161 (1988).
88. G. Hans, *Carbohydrate Research* **118**, 255 (1983).
89. Y. Fang, S. Al-Assaf, G. O. Phillips, K. Nishinari, T. Funami *et al.*, *The Journal of Physical Chemistry B* **111**, 2456 (2007).
90. T. Takeuchi, Nibu, Yutaka, K. Murata, Yoshida *et al.*, *Food Science and Technology International, Tokyo* **3**, 388 (1997).
91. H. Chen, M. M. Rogalski, J. N. Anker, *Phys Chem Chem Phys Physical chemistry chemical physics : PCCP* **14**, 13469 (2012).
92. G. L. Liu, Y. Lu, J. Kim, J. C. Doll, L. P. Lee, *Adv. Mater.* **17**, 2683 (2005).
93. M. Geiser, *J Aerosol Med Pulm Drug Deliv* **23**, 207 (2010).
94. J. A. Alberts B, Lewis J, *et al.*, in *Chapter 13: Intracellular Vesicular Traffic*, N. Y. G. S., Ed. (2008), pp. 749-812.
95. D. H. Bowden, *Experimental lung research* **12**, 89 (1987).
96. J. A. Swanson, *Nature reviews Molecular cell biology* **9**, 639 (2008).
97. M. Geiser, *Microscopy research and technique* **57**, 512 (2002).
98. K. Kwiatkowska, A. Sobota, *Bioessays* **21**, 422 (1999).
99. J. A. Alberts B, Lewis J, *et al.*, in *Chapter 16: They Cytoskeleton*, N. Y. G. Science, Ed. (2008), pp. 965-1052.
100. H. E. Huxley, *Science* **164**, 1356 (1969).
101. A. Yildiz, J. N. Forkey, S. A. Mckinney, T. Ha, Y. E. Goldman *et al.*, *science* **300**, 2061 (2003).
102. N. Hirokawa, *Science* **279**, 519 (1998).
103. A. Yildiz, P. R. Selvin, *Trends in cell biology* **15**, 112 (2005).
104. S. A. Burgess, M. L. Walker, H. Sakakibara, P. J. Knight, K. Oiwa, *Nature* **421**, 715 (2003).
105. S. L. Reck-Peterson, A. Yildiz, A. P. Carter, A. Gennerich, N. Zhang *et al.*, *Cell* **126**, 335 (2006).
106. M. Aridor, L. A. Hannan, *Traffic* **1**, 836 (2000).
107. M. Aridor, L. A. Hannan, *Traffic* **3**, 781 (2002).
108. S. H. Cheng, R. J. Gregory, J. Marshall, S. Paul, D. W. Souza *et al.*, *Cell* **63**, 827 (1990).
109. K. J. De Vos, A. J. Grierson, S. Ackerley, C. C. J. Miller, *Annu. Rev. Neurosci.* **31**, 151 (2008).

110. S. Roy, B. Zhang, V. M.-Y. Lee, J. Q. Trojanowski, *Acta Neuropathol* **109**, 5 (2005).
111. D. McDonald, M. A. Vodicka, G. Lucero, T. M. Svitkina, G. G. Borisy *et al.*, *The Journal of cell biology* **159**, 441 (2002).
112. E. M. Damm, L. Pelkmans, *Cellular microbiology* **8**, 1219 (2006).
113. G. L. Abrahams, M. Hensel, *Cellular microbiology* **8**, 728 (2006).
114. R. D. Vale, *Cell* **112**, 467 (2003).
115. R. Y. Tsien, *Nature Reviews Molecular Cell Biology* **4**, SS16–SS21 (2003).
116. J. A. Alberts B, Lewis J, *et al.*, in *Chapter 9: Visualizing Cells*, N. Y. G. S., Ed. (2008), pp. 579-616.
117. R. Hooke, *Micrographia: or some physiological descriptions of minute bodies made by magnifying glasses, with observations and inquiries thereupon* (Courier Corporation, 2003), pp. 131-138.
118. F. Zernike, *Physica* **9**, 974 (1942).
119. S. Inoué, *Chromosoma* **5**, 487 (1953).
120. R. D. Allen, N. S. Allen, J. L. Travis, *Cell motility* **1**, 291 (1981).
121. R. D. Allen, J. Metuzals, I. Tasaki, S. T. Brady, S. P. Gilbert, *Science* **218**, 1127 (1982).
122. E. D. Salmon, *Trends in cell biology* **5**, 154 (1995).
123. R. D. Vale, *Annual review of cell biology* **3**, 347 (1987).
124. R. D. Vale, B. J. Schnapp, T. S. Reese, M. P. Sheetz, *Cell* **40**, 449 (1985).
125. N. Flores-Rodriguez, S. S. Rogers, D. A. Kenwright, T. A. Waigh, P. G. Woodman *et al.*, *PloS one* **6**, e24479 (2011).
126. B. Cui, C. Wu, L. Chen, A. Ramirez, E. L. Bearer *et al.*, *Proceedings of the National Academy of Sciences* **104**, 13666 (2007).
127. A. L. Zajac, Y. E. Goldman, E. L. F. Holzbaur, E. M. Ostap, *Current Biology* **23**, 1173 (2013).
128. Y. Gu, W. Sun, G. Wang, K. Jeftinija, S. Jeftinija *et al.*, *Nature communications* **3**, 1030 (2012).
129. V. G. Allfrey, A. E. Mirsky, *Proceedings of the National Academy of Sciences of the United States of America* **43**, 589 (1957).
130. A. N. Wick, D. R. Drury, H. I. Nakada, J. B. Wolfe, *Journal of Biological Chemistry* **224**, 963 (1957).
131. H. Imamura, K. P. H. Nhat, H. Togawa, K. Saito, R. Iino *et al.*, *Proceedings of the National Academy of Sciences* **106**, 15651 (2009).
132. H. Watanabe, W. Kuhne, R. Spahr, P. Schwartz, H. M. Piper, *American Journal of Physiology-Heart and Circulatory Physiology* **260**, H1344 (1991).
133. S. Lin, *Fluorescent Methods for Investigating Metabolic Processes in Trypanosoma Brucei* (2015).
134. I. Nemoto, T. Takahashi, T. Matsuzaki, *Engineering in Medicine and Biology Society IEEE* **3**, 2963 (2001).
135. I. Nemoto, K. Ogura, H. Toyotama, *IEEE Trans. Biomed. Eng.* **36**, 598 (1989).
136. J. D. Brain, *Comprehensive Physiology* 447 (1985).

137. Z. Yang, K. T. Nguyen, H. Chen, H. Qian, L. P. Fernando *et al.*, *The Journal of Physical Chemistry Letters* **2**, 1742 (2011).